IJE TRANSACTIONS B: Applications Vol. 39, No. 11, (November 2026) 2690-2711

International Journal of Engineering

Journal Homepage: www.ije.ir

On the Post-aging of the ARB Created AA1050\AA2024$_{(pre-aged)}$\Al_2O_3 Composites

H. Roghani*[a,b], H. Partoyar[b], H. R. Jafarian[b], S. K. Sadrnezhaad[c], E. Borhani[a]

[a] *Nanomaterials Department, Faculty of New Sciences and Technologies, Semnan University, Semnan, Iran*
[b] *School of Metallurgy and Materials Engineering, Iran University of Science and Technology (IUST), Tehran, Iran*
[c] *Department of Materials Science and Engineering, Sharif University of Technology, Tehran, Iran*

PAPER INFO

Paper history:
Received 20 July 2025
Received in revised form 09 December 2025
Accepted 30 January 2026

Keywords:
Aluminum
Accumulative Roll Bonding
Aging Process
Nanocomposites
Alumina

ABSTRACT

In this study, multilayered aluminum-based composites consisting of AA1050 (66.6 vol.%) and pre-aged AA2024 (33.4 vol.%) with a trace addition of Al_2O_3 nanoparticles (0.005 vol.%) were successfully fabricated using six cycles of accumulative roll bonding (ARB). The composites were subsequently subjected to post-aging at 110, 150, and 190 °C for varying durations (0–10 h) to optimize their microstructural and mechanical performance. A combination of optical microscopy, SEM, TEM, microhardness, and tensile testing was employed to evaluate the materials. The results revealed that ARB, in combination with minimal nanoparticle reinforcement, led to significant grain refinement. Remarkable enhancements in tensile strength (up to 220 MPa, a 215% increase over annealed AA1050) and ductility (14% total elongation) were achieved by ARB and post-aging. Notably, the presence of alumina nanoparticles not only delayed over-aging but also contributed to improve particle–matrix bonding and structural stability. This work introduces a practical approach for tailoring high-performance aluminum composites via hybrid strategies involving ARB, precipitation hardening, and nanoparticle-assisted microstructure refinement.

***doi**: 10.5829/ije.2026.39.11b.04*

Graphical Abstract

TEM image of six stages ARBed AA1050\AA2024\Al_2O_3 composite, a) AA1050 area, b) AA2024 fragment

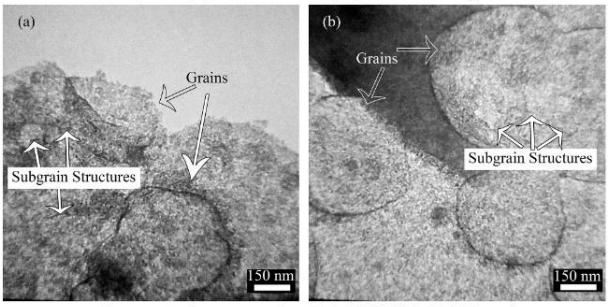

Stress-strain curves for a) AA2024\AA1050 and, AA2024\AA1050\$Al_2O_3$ composites created by six stages of ARB b) heat treated AA1050\AA2024\$Al_2O_3$ composites at 110 °C,

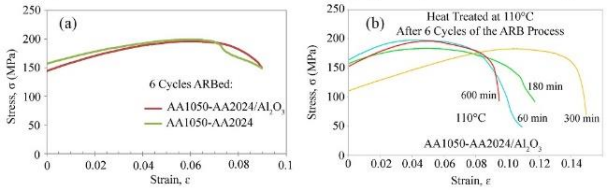

*Corresponding Author Email: hamed_roghani@mail.iust.ac.ir, hamed.roghani@gmail.com (H. Roghani)

Please cite this article as: Roghani H, Partoyar H, Jafarian HR, Sadrnezhaad SKh, Borhani E. On the Post-aging of the ARB Created AA1050\AA2024$_{(pre-aged)}$\Al_2O_3 Composites. International Journal of Engineering, Transactions B: Applications. 2026;39(11):2690-711.

1. INTRODUCTION

Due to its light weight, high strength-to-weight ratio, and availability, aluminum is used in many industries, including automobiles, ships, and aviation. However, because aluminum is weaker than alloys such as steel, there has always been a need to increase its strength. Various methods, such as alloying, aging, work hardening, and composite formation, are used to improve aluminum's strength. Of course, each method has its use in improving specific features. However, by combining the four methods—alloying, work hardening, aging, and composite making —it is possible to create an aluminum-based material with improved all-around properties (1-4).

Aluminum alloy series 1000 and 2000 are near pure aluminum and copper-containing alloys, respectively. The aluminum 1000 series has low strength, and the only way to increase it is through fine-graining and work hardening. The 2000 series alloys can be age-hardened to increase their strength and hardness. However, 2000 series alloys are unsuitable for ambient-temperature rolling and are more expensive than 1000 series alloys (5-8). It is possible to leverage the rolling ability and low cost of the 1000 series, and the high hardness and strength of the 2000 series, by combining the 1000 and 2000 series as a composite.

ARB is a suitable method for fine-graining and increasing the work hardening of metal sheets. By doing several stages of ARB, an ultrafine-grained (UFG) structure can be achieved. In the UGF structure, the grain size is less than 1 micron. It is usually necessary to perform 5 ARB stages with a 50% thickness reduction to create the UFG structure. However, the aging ability of the alloy, the rolling temperature, and the composite-making process affect the number of ARB stages required to obtain a UFG structure (8-12).

By ARB, layered composites such as Al/Cu/Zn/Ni (13), Al/Ni-SiC (14), and metal base composites with ceramic reinforcing particles such as Al-SiC/graphene (15), Al-B_4C (16), AA1100/Fe_2O_3 (17), Pb/W-Co_3O_4 (18), AA5052-GO (19), Cu-GO (20) and Al-MWCNT/Al_2O_3 (21) were created. The bonding of the reinforcing particles and the metal matrix and metal layers is mechanical. Mechanical bonding and work hardening accumulation during ARB reduce the elongation and ductility of the product. Elongation can be improved while maintaining tensile strength by performing and optimizing the post-ARB heat treatment. This is one of the cases we investigated.

Most research on composite making using the ARB method has used 1-4% reinforcing particles. In more than 4% of reinforced particles, the bonding between layers is not well established by ARB. Also, composite sheets become very prone to cracking. We successfully tested the addition of 0.5 vol.% of CuO nanoparticles. However, according to our results (3, 9) and the calculations of Reihanian et al. (22), we concluded that a minimal amount of reinforcing nanoparticles can have a significant effect on the microstructure and mechanical properties in much fewer cycles due to the high surface-to-volume ratio of nanoparticles. For this reason, 0.005 vol% alumina was used as reinforcement in this project. The effect of using minimal reinforcing particles has not been researched. Also, due to the high roller pressure during ARB, the agglomerated particles are separated. Therefore, we used inexpensive, reinforcing agglomerated nanoparticles to reduce production costs.

Heat treatment for age-hardenable metals causes precipitates and increases hardness and strength. However, there is an optimal temperature and time for heat treatment on metals with aging capability. Also, heat treatment of non-age-hardenable metals can cause recovery or recrystallization, thereby decreasing strength and hardness. Of course, treatment also increases ductility. In a layered composite, determining the optimal temperature and time of heat treatment to achieve the desired tensile strength, hardness, and ductility is crucial (6, 23-27).

Aging before and after ARB can significantly affect microstructural and mechanical properties. The effect of rolling on the post-aging of aluminum-copper alloys has already been researched by Zheng et al. (28) and Tsuji et al. (29). In a study conducted by Tsuji et al. (29) on the ARB-ed Al-2 wt.% Cu alloy, post-aging at 190°C reduced the hardness, but Zheng et al. (28) showed that by reducing the aging temperature to 100°C, the hardness of ARBed AA2024 alloy could be increased. Also, Rezaei et al. (30) increased the total elongation from 5% to 9% by performing post-aging at 100°C on a five-cycle ARB-ed AA6061 alloy. However, the effect of ARB on the post-aging of pre-aged aluminum-copper alloys that were then ARBed has not been studied. Also, the heat treatment of the layered composite reinforced with ARB-created particles has not been investigated. This is a key point in our research, where we try to improve the strength and elongation of the composite by optimal aging and take a practical step towards the application of ARB-ed aluminum.

In this research, we attempted to increase the tensile strength, total elongation, and hardness of AA1050. For this purpose, we created AA1050 (66.6 vol.%)\AA2024 (33.4 vol.%) and AA1050(66.6 vol.%)\ AA2024(33.4 vol.%)\$Al_2O_3$ composites with six ARB stages. To prepare the AA1050\AA2024\$Al_2O_3$ composite, very negligible Al_2O_3 (0.005 vol.%) and aged AA2024 alloy were used. For the first time, we investigated the effect of pre- and post-aging on a hybrid composite produced by the ARB method. For this purpose, we subjected the composite to heat treatment at various times and temperatures to determine the optimal aging time and

temperature for improved mechanical properties. In this way, we investigated the microstructure and the mechanisms of change in mechanical properties.

2. MATERIALS AND METHODS

To create AA1050\AA2024\Al_2O_3 composite, AA1050 (Iranian Aluminium Co. (IRALCO)) and AA2024 (Panache Industries Co.) sheets with respective thickness, width, and length of 0.7, 40, and 80 mm were used, respectively. Alumina sub-micron particles (Nanochemazone Co.) were used to reinforce the samples. The chemical composition of the used aluminum alloy sheets is shown in Table 1. The elemental values were obtained by spark emission spectroscopy using a Hitachi High-Tech FOUNDRY-MASTER Smart instrument. The measurement accuracy was four decimal places. In addition, the XRD pattern of alumina nanoparticles and their SEM image are shown in Figure 1. In this project, agglomerated alumina nanoparticles were used to reduce production costs.

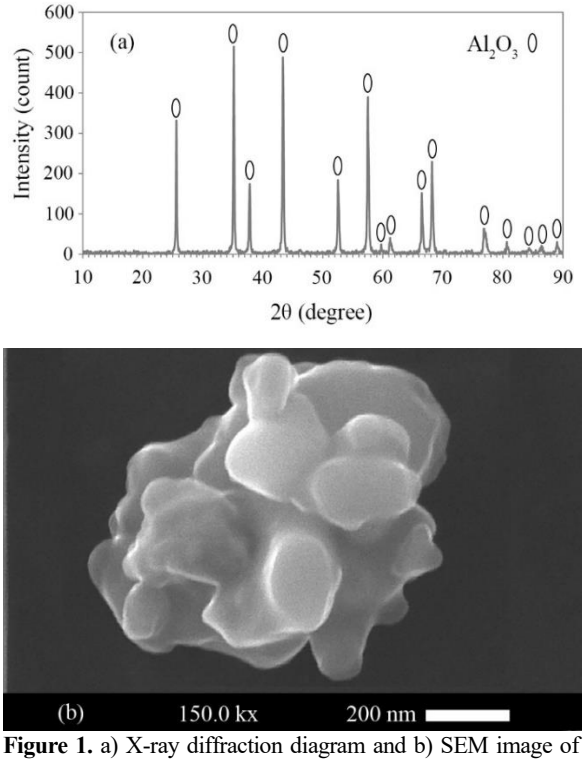

Figure 1. a) X-ray diffraction diagram and b) SEM image of Al_2O_3 particles

The annealing processes for AA1050 and AA2024 were performed at 370 ± 5 °C and 500 ± 5 °C for 6 h (9) and 2 h (28), respectively. After annealing, all sheets were cooled in water (water quench). Next, the AA2024 sheets were age-hardened for 30 minutes at 190 ± 3 °C (31) to form nanometer-sized S' precipitates. Age hardening was done directly after quenching (to prevent natural aging) in an ambient atmosphere in the electric oven.

After the annealing and aging, a sheet of aluminum alloy 2024 was sandwiched between 2 sheets of AA1050. To bond layers and clean the surface sheets of oxidation and pollutants, a metal brush was used to remove dirt and surface oxidation. To prevent the reformation of surface oxides, the sheets were prepared and then rolled with a short interval. At both ends, the sheets were fixed by a metal wire. In this way, the set of sheets was ready for rolling. We used a laboratory rolling machine with a rotation speed of 12 rpm and a 360 mm roller diameter. The rolling machine had two rollers. Also, the rolling process was carried out without lubricant and at ambient temperature. Rolling was performed with a 50% thickness reduction. We cut the rolled sheet in half. Afterward, surface preparation, stacking, wire fixing, and rolling were repeated. In total, six ARB stages were performed. ARB is schematically shown in our previous work (9). Suspension containing acetone and alumina (0.005 vol.%) was sprayed on two surfaces of AA2024 before the first stage of ARB to investigate the effects of using Al_2O_3. Figure 2 shows an AA2024 sheet brushed and then layered. After performing 6 ARB stages, different temperatures and aging times were tested (as shown in Table 2). We determined the temperatures based on the typical aging temperature of AA2024 (190 °C), the temperature introduced by Tsuji's team (about 100 °C) (29), and an intermediate temperature (150 °C).

Phase analysis was done using a Philips Co. XRD device (Cu Kα target, PW 3710 model). To investigate the microstructure, we used an optical microscope (Leitz Metallux 3), a scanning electron microscope (FESEM, TESCAN Co., MIRA3-XM model, with an acceleration voltage of 15.0 kV), and a transmission electron microscope (TEM, Philips CM30). If etching is needed, we used Keller's solution (190 ml distilled water, 2 ml hydrofluoric acid, 5 ml nitric acid, and 3 ml hydrochloric acid).

Mechanical properties were measured using standard techniques, including micro-hardness (with a Matsuzawa

TABLE 1. Elemental composition (wt.%) of AA2024 and AA1050 sheets used in this research

Alloy	Elements	Al	Cu	Mg	Fe	Si	Zn	Mn
Aluminum alloy - 1050	Wt.%	Balance	0.016	0.008	0.289	0.062	0.027	0.010
Aluminum alloy - 2024	Wt.%	Balance	4.25	1.628	0.109	0.0746	0.115	0.437

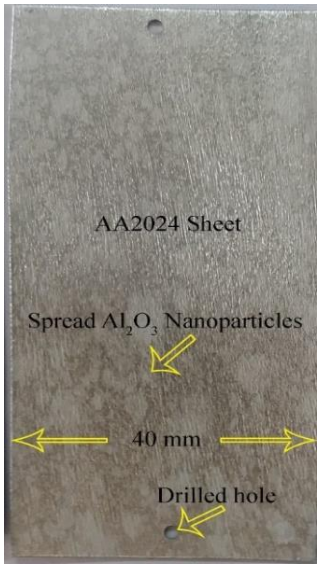

Figure 2. A ready AA2024 sheet for ARB

TABLE 2. Aging time and temperatures (positive sign means heat treatment, and negative sign means no heat treatment)

Temperature (°C) \ Time (min)	10	30	60	180	300	600
110	-	-	+	+	+	+
150	+	+	+	+	-	-
190	+	+	+	+	-	-

MMT machine at 0.98 N force and 15 s indentation time) and tensile strength (with a Sanaf SUT-500k at a strain rate of 8.3×10^{-4} s^{-1}). To measure the microhardness of each sample, we adhered to the JIS Z2201 standard (31), measuring the hardness at 5 points on the ND-RD plane (from the surface to the middle of the sheet) and reporting the average. Tensile test bone-shaped specimens were created by wire-cutting in the rolling direction, with a gauge length of 4 mm, following the same standard.

We did not use an extensometer during the tensile test. For this reason, the diagrams' elastic modulus is invalid. Not using an extensometer was due to the small and miniature dimensions of the tensile test specimens. To measure total elongation, we measured the specimen's length before and after the tensile test. Thus, the total elongation was obtained. We obtained the percentage of total elongation by dividing the change in length by the gauge length and multiplying the ratio by 100.

3. RESULTS

3. 1. Microstructure of ARBed Composites

Figure 3 shows the metallographic image of aluminum alloy 2024 after annealing. In this image, equiaxed grains ranging in size from 5 to 40 µm are visible. Annealed AA1050 has almost equiaxed grains with diameters ranging from 2 to 30 µm, as reported in our previous work (7, 9). In this way, the annealing heat treatment has eliminated the effect of mechanical work during the creation of the aluminum sheet.

The SEM image of the AA1050\AA2024\Al_2O_3 nanocomposite after 1, 3, and 6 ARB stages and the AA1050\AA2024 composite after 6 ARB stages are shown in Figure 4. Precipitates are visible in the field of AA2024. According to scientific literature, distinct precipitates form in aluminum alloys containing copper and magnesium (4, 25, 32). The precipitates visible in the SEM of aluminum alloy 2024 include T-phase particles ($Al_{20}Cu_2Mn_3$) (32, 33), types of GPB and GP (4, 25), S and S' (Al_2CuMg) precipitates (4, 33). These precipitates were not formed during aging. According to previous studies, at 190 °C and 30 minutes, precipitates below 100 nm are formed (31).

After the first and third ARB stages, microcracks (in the rolling direction) formed between the AA1050 and AA2024 layers due to poor bonding. Incomplete bonding between the AA2024 and AA1050 layers was not observed in the AA1050\AA2024 composite prepared via 6 ARB steps. However, cracks (45° to the rolling direction) were observed in AA2024 parts of the AA1050/AA2024/Al_2O_3 composite processed with six ARB stages, due to the breaking of the AA2024 layers. The failure of the layers occurred at an angle of about 45°. The surfaces of the broken layers were elongated and had different angles when performing several stages of ARB.

The total sheet thickness was reduced by 50% at each ARB stage. Thus, it was expected that, by performing six ARB steps, the thickness of the AA2024 layers would

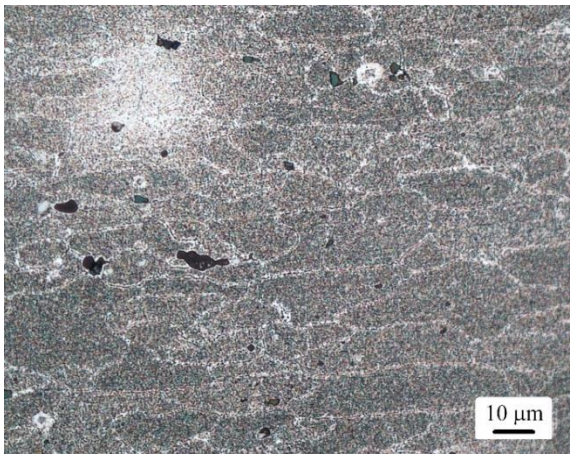

Figure 3. Metallographic image of AA2024 (after annealing)

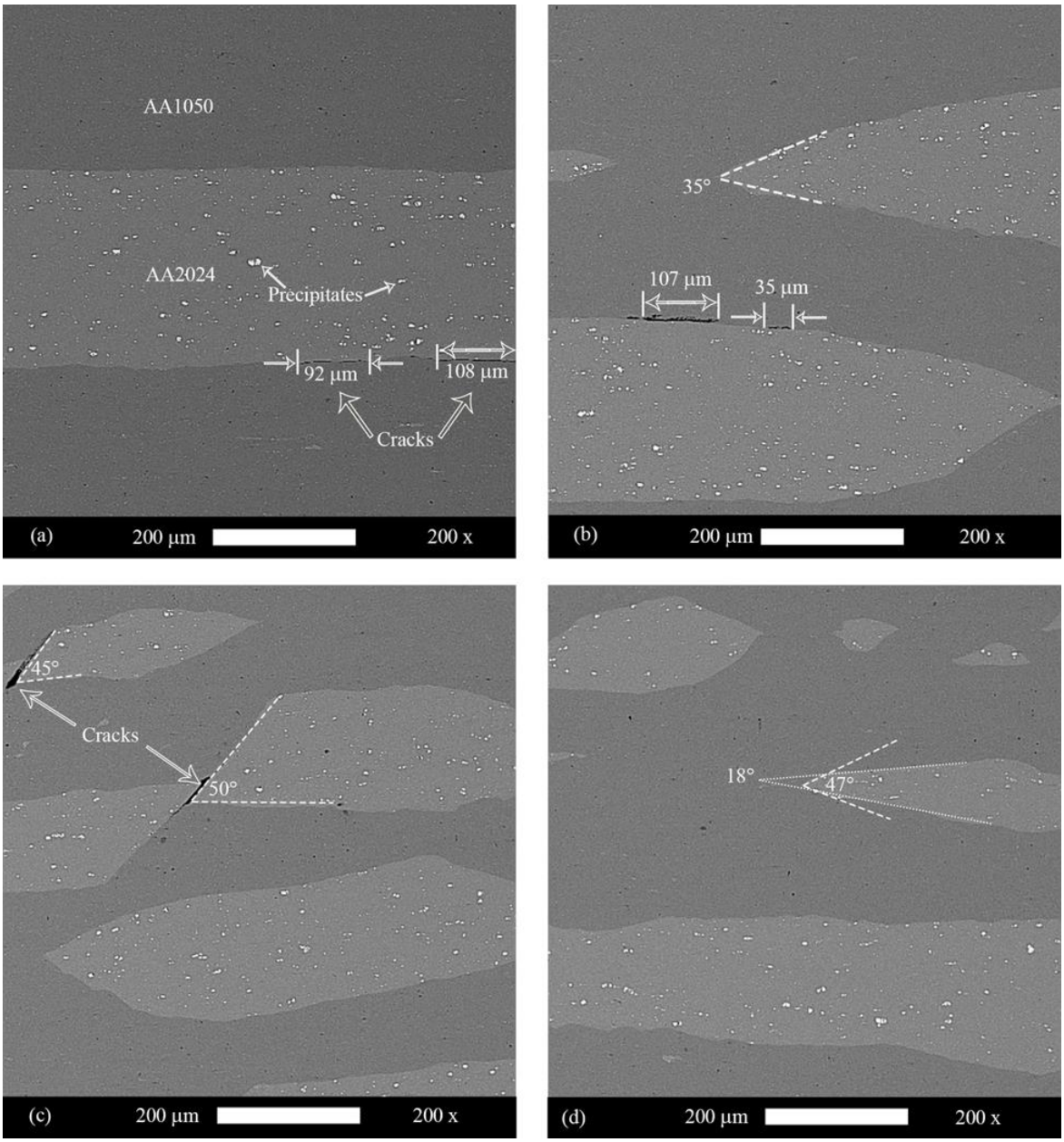

Figure 4. Backscattered electrons SEM image from AA1050\AA2024\Al_2O_3 composite after a) one, b) three, and c) six ARB stages and d) AA1050\AA2024 composite after 6 ARB stages

reach 11 µm from an initial thickness of about 700 µm. However, the thickness of AA2024 layers after six ARB stages was about 170 µm. Therefore, it was concluded that a strain much lower than the rolling strain (strain equivalent to 4.8) was applied to the AA2024 layers. According to the calculations, a strain equivalent to 2 stages of ARB (1.6) was applied to the large AA2024 pieces.

As stated in the experimental section, we added 0.005% alumina by volume to the composite during the first stage of the ARB process. Due to the low alumina content, EDS-MAP analysis was performed to identify alumina within the structure. The SEM image and the related EDS-MAP analysis are shown in Figure 5. These images show oxygen accumulation and a slight decrease in aluminum intensity at the boundary between the AA2024 and AA1050 layers. The accumulation of oxygen and a decrease in aluminum intensity indicate the presence of alumina. Alumina was penetrated at two layers, AA1050 and AA2024. However, more penetration of alumina in the AA1050 layer was observed (Figure 5). The uniform oxygen distribution in Figure 5

shows the proper distribution of Al_2O_3 nanoparticles in the boundaries of the AA2024 and AA1050 layers.

The elemental distribution map is shown in Figure 5. However, to illustrate the elements numerically, the EDS analysis of points 1 and 2, marked in Figure 5, is presented in Figure 6. As can be seen, oxygen that reason for existence of alumina was detected by EDS analysis in the oxygen concentration region of Figure 5. However, at the point outside the oxygen concentration region of MAP of Figure 5, the oxygen element was not detected. Therefore, although alumina particles were not observed in the SEM analysis, their presence was confirmed in the EDS and EDS-MAP analyses.

The EDS analysis results in Figure 6 differ from those in Table 1, even though both show the percentages of elements in the sheets. There are several reasons for this. In fact, Table 1 is expressed in mass percent, whereas the tables in Figure 6 are expressed in atomic percent. By converting, the difference is reduced but still significant. In fact, the two tests, EDS and spark emission spectroscopy, differ in nature. Also, EDS examines a small area of the sample, whereas spark emission spectroscopy examines a large area of the sheet surface. Finally, spark emission spectroscopy is reliable for analyzing the elemental composition of a metal sample, and EDS is suitable for examining and comparing features observed in microscopic images.

Figure 7 shows an image of a nanoparticle among AA1050 grains from a six-stage ARB-ed AA1050\AA2024\Al_2O_3 composite. Because the AA1050 alloy does not age harden, and we only used alumina nanoparticles, we most likely identified this particle as alumina. Therefore, the agglomeration of alumina particles has disappeared, and alumina particles with a maximum surface dimension of 200 nm and a thickness of about 50 nm are present as completely separate particles in the composite. The alumina particles initially used were agglomerated; however, applying pressure during rolling disrupted the agglomeration, allowing the particles to be properly distributed individually. Due to the high strength of alumina particles compared to aluminum and the aluminum flowing around them, these particles did not break (9, 34).

TEM analysis was performed to investigate the precipitation during the aging process. Figure 8 shows the TEM image of aluminum alloy 2024 annealed and

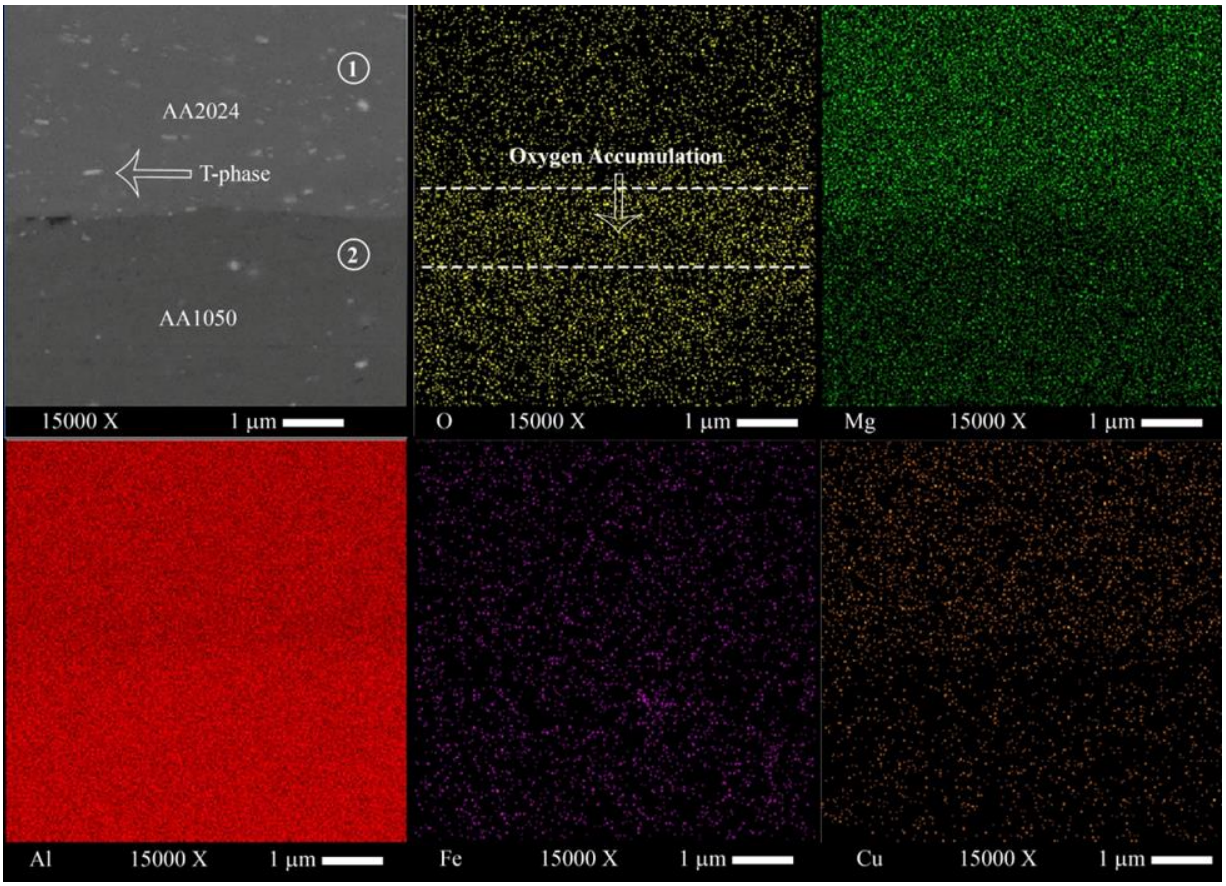

Figure 5. SEM image (backscattered electron) and EDS-MAP analysis of the AA1050\AA2024\Al_2O_3 composite after one ARB stage

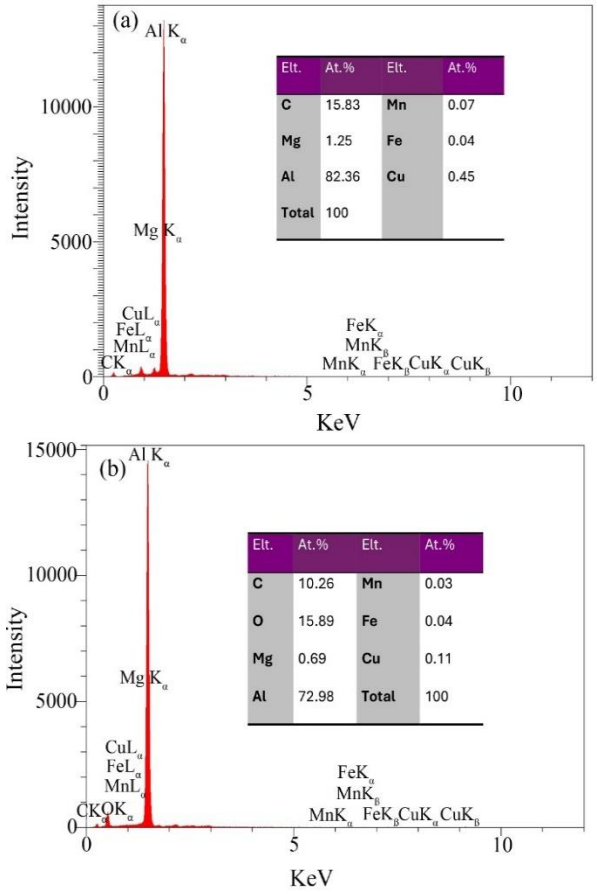

Figure 6. EDS analysis and corresponding elemental table of a) point 1 and b) point 2 from the SEM image of Fig 5.

then age-hardened. Dark-field TEM image of Figure 8(b) shows some nanoscale precipitates (S' precipitates) that

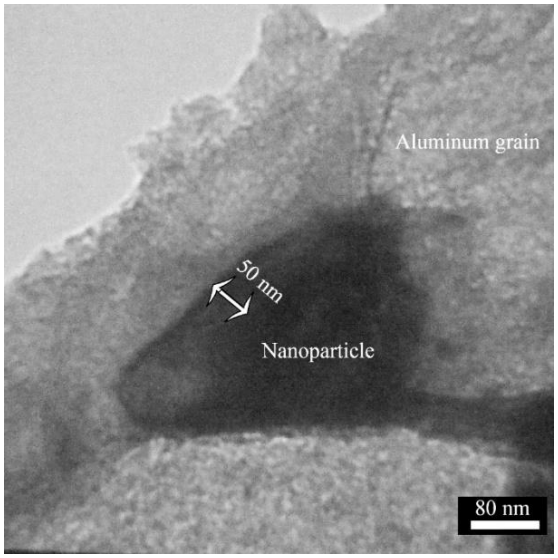

Figure 7. TEM image of nanoparticle in the AA1050\AA2024\Al_2O_3 composite after six ARB stage

are not well visible in the bright-field TEM image (Figure 8(a)). The dark-field TEM image shows the reflection from a specific crystallographic plane, enabling the detection of precipitates within the metal matrix.

Electrons passing through the sample create the bright-field image. Thus, precipitates with a composition similar to that of the metal matrix do not provide good contrast in a bright-field image. However, due to differences in the crystallinity parameters of the precipitate and the metal matrix, the precipitate reflects the electron beam at a different angle and with greater intensity. Thus, precipitates can be detected in the dark-field image (35, 36).

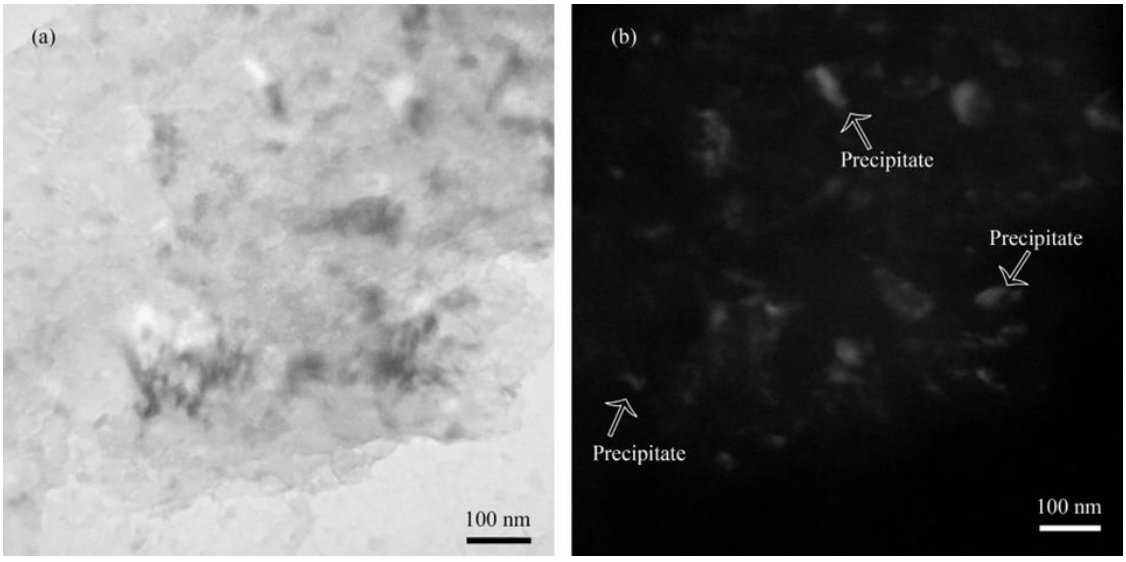

Figure 8. TEM image of a) bright field and b) dark field of annealed and then aged AA2024

In the dark-field TEM image of Figure 8, S' precipitates range in length from 30 nm to 130 nm. These precipitates were formed during the pre-aging process, which was carried out for 30 minutes at 190 °C, depending on precipitate size and scientific references (25, 31).

In order to investigate grain refinement during ARB, TEM analysis was performed on two composites of AA1050\AA2024\$Al_2O_3$ and AA1050\AA2024. Figure 9 shows the TEM images of the mentioned composites in AA2024 fragments and AA1050 layers. The grains in the AA1050\AA2024\$Al_2O_3$ and AA1050\AA2024 composites had apparent differences. Aluminum grains in the composite with alumina were equiaxed, whereas those in the composite without reinforcing particles were elongated. The grains in the composite containing alumina nanoparticles were smaller than those in the AA1050\AA2024 composite.

In TEM images, it was observed that the grains of AA1050 in the composite containing alumina nanoparticles were between 200 and 400 nm in size, while the grain size in AA2024 was between 300 and 600 nm. Both alloys showed numerous subgrains, and since the grains of AA1050 were smaller than those of AA2024, AA1050 had a higher number of subgrain structures. Of course, the TEM images only show a small part of the sample. To reduce this weakness, we imaged several different locations of the samples and obtained grain sizes within the mentioned ranges.

Precipitates of more than 100 nm are visible in Figures 4 and 9. Therefore, ARB did not remove deposits containing copper. To investigate the remaining nanometer precipitates after six ARB stages, additional analyses were conducted. Figure 10 shows the TEM image of S' nanometer precipitates in the AA1050\AA2024\Al_2O_3 composite created with 6 ARB stages. In the bright-field image (Figure 10(a)), nanometer precipitates are difficult to distinguish, whereas in the dark-field image (Figure 10(b)), S' nanometer precipitates are visible. That shows the lack of impact of ARB on copper-containing nanometer precipitates.

3. 2. Microstructure after Post-age Hardening

After 6 ARB steps, the composites were age-hardened at different temperatures and times. Table 2 (in the experimental section) shows the aging temperatures and times. Figure 11 shows SEM images of the composites AA1050\AA2024 and AA1050\AA2024\Al_2O_3 after aging at 110 °C for 3 and 10 h. As expected, the SEM

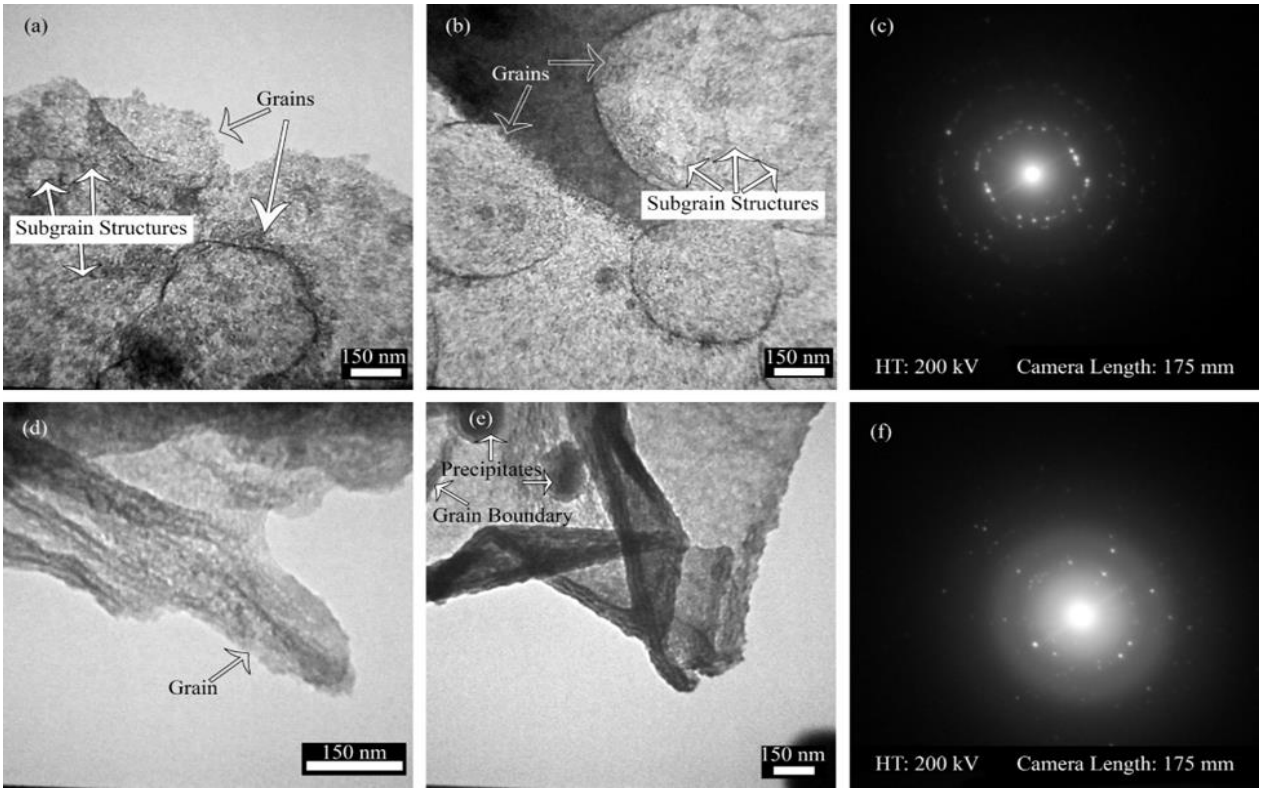

Figure 9. TEM image of six stages ARBed AA1050\AA2024\Al_2O_3 composite, a) AA1050 area, b) AA2024 fragment and c) selected area diffraction (SAD) from a and b, TEM image of six stages ARBed AA1050\AA2024 composite, d) AA1050 area, e) AA2024 fragment and f) SAD from d and e

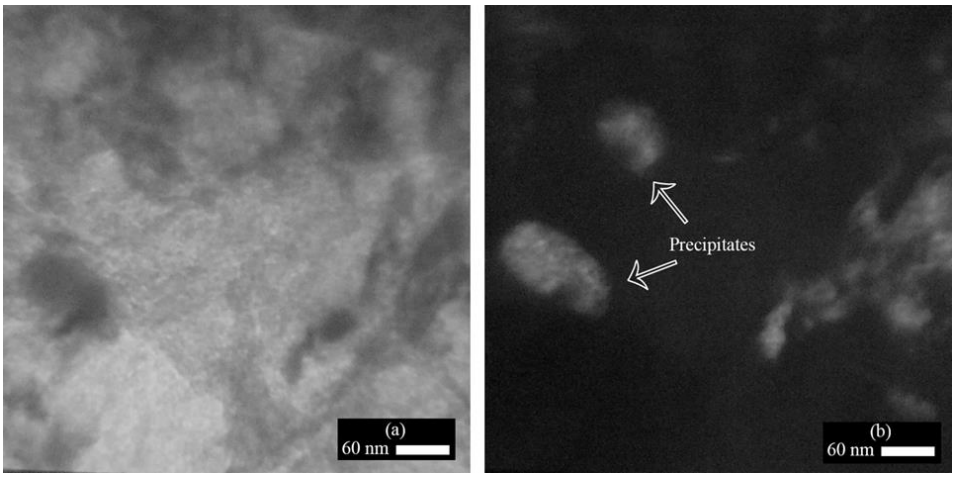

Figure 10. TEM image of a) bright field and b) dark field of AA1050\AA2024\Al_2O_3 composite after six ARB stages

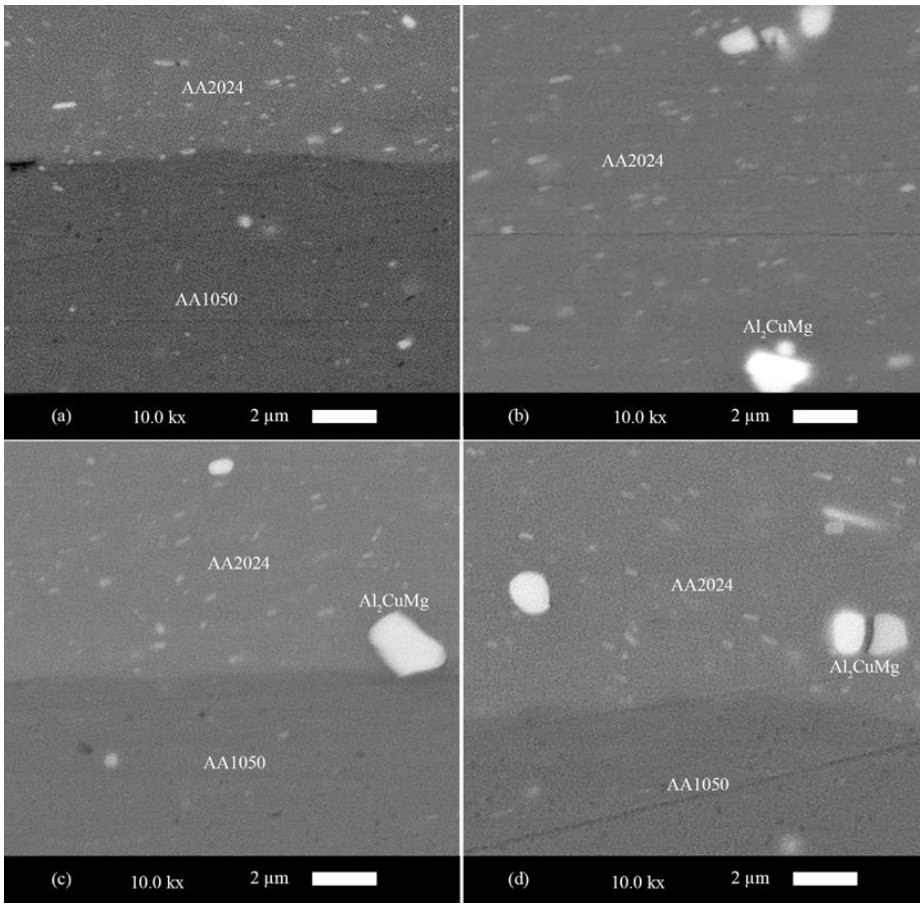

Figure 11. SEM image after aging at 110°C for a) 3 hours of AA1050\AA2024\$Al_2O_3$ composite, b) 10 hours of AA1050\AA2024\$Al_2O_3$ composite, c) 3 hours of AA1050\AA2024 composite, and d) 10 hours of AA1050\AA2024 composite

images showed no changes or precipitation in the AA1050 layers. As expected, the SEM images showed no changes or precipitation in the AA1050 layers. No precipitation in AA1050 is because AA1050 is almost pure aluminum. However, precipitation was observed in the AA2024 layers. These precipitations mainly consisted of T-phase and Al_2CuMg precipitates. As the aging time increased, the number and size of precipitates increased. The precipitation in the AA1050\AA2024

composite proceeded faster than the AA1050\AA2024\Al_2O_3 composite.

Because the SEM images provided reasonable information about the post-aged composites and because the chosen temperatures were not at the level of recrystallization or grain growth, we refrained from performing further microscopic analyses of the ARB-ed and post-aged composites. We focused our attention at this stage on performing and discussing mechanical tests.

3. 3. Mechanical Properties Heat treatment at different times and temperatures was performed on the AA1050/AA2024 composite, prepared from aged AA2024 with or without alumina particles. Microhardness and tensile strength were measured to investigate the effect of heat treatment on the mechanical properties of the created composite. The fracture surface of the composites was then investigated. The results of these tests are shown below.

Figure 12 illustrates the results of microhardness analysis for AA1050\AA2024 and AA1050\AA2024\Al_2O_3 composites after heat treatment at different temperatures and times. As shown in Figure 12, heat treatment did not significantly affect the hardness of AA1050 layers. However, a substantial increase of 40% or more in microhardness was observed compared to annealed AA1050. This increase was primarily due to the creation of the UFG structure by the ARB process (Figure 9), a significant scientific finding that played a crucial role in the observed increase in microhardness since the work hardening caused by rolling is expected to be significantly reduced by thermal treatment at temperatures of 110–190°C for up to 10 hours (7, 37).

However, the microhardness of AA2024 layers had significant changes. All the microhardness graphs showed an increasing peak that occurred more rapidly at higher temperatures. The hardness-increase peak is associated with the deposition of Al_2CuMg in AA2024 layers (28, 29). Notably, the peak in heat-treatment hardness for the AA1050\AA2024 composite occurred at 110 °C in less time than for the AA1050\AA2024\Al_2O_3 composite.

The stress-strain curves for annealed AA1050, annealed and aged AA2024, AA1050\AA2024, and AA1050\AA2024\Al_2O_3 composites created by ARB are shown in Figures 13(a) and 13(b). Also, the stress-strain diagrams of the composites subjected to different heat treatments are shown in Figures 13(c) to 13(f). These diagrams show that ARB caused a sharp decrease in strain. However, the ultimate tensile strength (UTS) of composites created with six ARB stages increased more than 2.5 times compared to annealed AA1050. Also, the strength and elongation of the heat-treated composites oscillated. Examining these changes and identifying a logical relationship between heat treatment and changes in tensile properties requires comparing the variables of total elongation and tensile strength across different samples.

Figures 14(a), 14(b) and 14(c) show the changes in total elongation, yield strength (YS) and UTS for the created AA1050\AA2024 and AA1050\AA2024\Al_2O_3 composites, and then subjected to heat treatment. In the charts of Figures 14 (a) and 14(b), it can be seen that heat treatment at different temperatures had a significant and equal effect on the UTS and elongation of the composites created by the ARB method. In all diagrams, the tensile strength first decreased slightly and then increased. Then, the tensile strength decreased again and reached a constant value. The decrease in tensile strength can be due to softening during heat treatment. Softening occurred during heat treatment, as some dislocations recovered. However, this recovery was insufficient to cause a significant reduction in hardness (Figure 12). By aging and considering the role of precipitates in increasing tensile strength, UTS increased. Furthermore, excessive aging led to a decline in tensile strength.

Figures 14 (a), 14(b) and 14(c) show the changes in total elongation, yield strength (YS) and UTS for the created AA1050\AA2024 and AA1050\AA2024\Al_2O_3 composites, and then subjected to heat treatment. In the charts of Figures 14 (a) and 14(b), it can be seen that heat treatment at different temperatures had a significant and equal effect on the UTS and elongation of the composites created by the ARB method. In all diagrams, the tensile strength first decreased slightly and then increased. Then, the tensile strength decreased again and reached a constant value. The decrease in tensile strength can be due to softening during heat treatment. Softening occurred during heat treatment, as some dislocations recovered. However, this recovery was insufficient to cause a significant reduction in hardness (Figure 12). By aging and considering the role of precipitates in increasing tensile strength, UTS increased. Furthermore, excessive aging led to a decline in tensile strength.

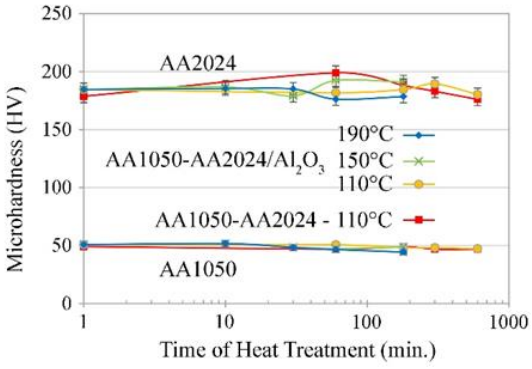

Figure 12. Microhardness analysis diagrams for AA1050\AA2024 and AA1050\AA2024\Al_2O_3 composites after heat treatment at various times and temperatures

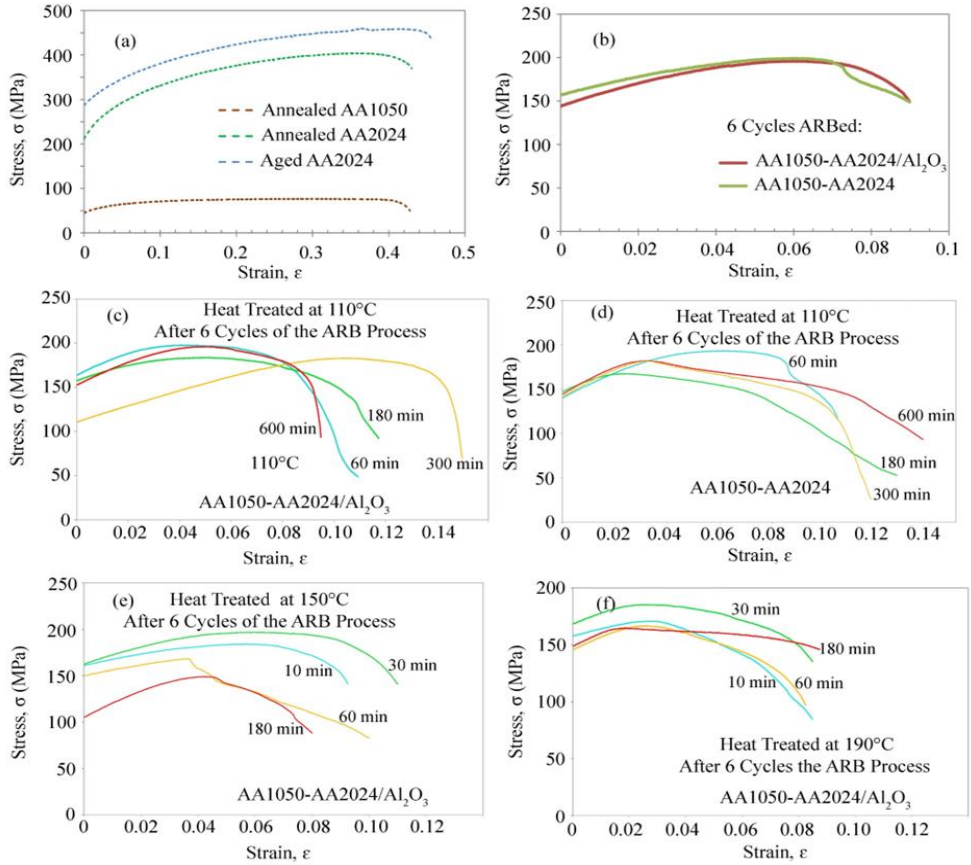

Figure 13. Stress-strain curves for a) AA2024 after annealing and aging, and AA1050 after annealing, b) AA2024\AA1050 and AA2024\AA1050\$Al_2O_3$ composites created by six stages of ARB, c) heat treated AA1050\AA2024\$Al_2O_3$ composites at 110 °C, d) heat treated AA1050\AA2024 composites at 110 °C, e) AA1050\AA2024\$Al_2O_3$ composites subjected to heat treatment at 150 °C and, f) AA1050\AA2024\$Al_2O_3$ composites subjected to heat treatment at 190 °C

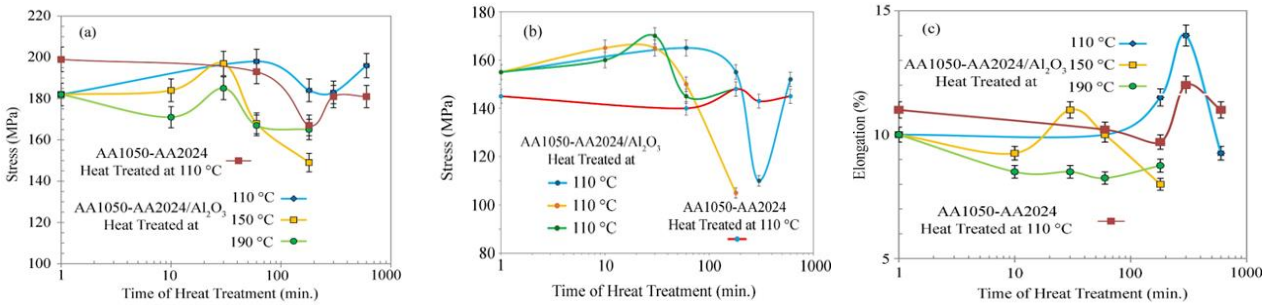

Figure 14. Diagrams of a) UTS, b) YS and c) total elongation for created AA1050\AA2024 and AA1050\AA2024\Al_2O_3 composites and then subjected to heat treatment

Elongation was also reduced, along with the initial reduction in tensile strength. Therefore, the initial recovery was insufficient to increase elongation. Also, with increasing tensile strength at longer heat-treatment times, elongation increased due to delayed rupture during tension. By increasing the heat treatment time, elongation exceeded the initial value before heat treatment in some cases, resulting in a final reduction in tensile strength. Long-term heat application could cause some recovery and increased elongation.

The presence or absence of alumina nanoparticles profoundly impacts the tensile strength and elongation of heat-treated composites. The AA1050\AA2024 composites' elongation and tensile strength, when heat-

treated at 110 °C, were lower than those of the AA1050\AA2024\Al_2O_3 composite under the same conditions. Access to higher tensile strength and elongation by using ceramic nanoparticles underscores the practical implications of our findings for materials science and engineering.

We calculated the strain hardening exponent (n) and other related parameters from the stress-strain curves in Figure 13 by calculating the logarithm of the Hollomon equation (Equation 1) (38, 39). To solve the Hollomon equation, we took Young's modulus to be 70 GPa, which is a reasonable range for aluminum. Then, we obtained the plastic strain by subtracting the elastic strain from the true strain (Equation 2). To ensure the accuracy of the calculations, the coefficient of determination (R2) was calculated for each sample (Equation 3). The coefficient of determination for all samples ranged from 0.93 to 1. This indicates the accuracy of the fit according to the Hollomon equation. The strain hardening exponent was calculated for each sample at 20 points in the linear plastic region. The results of these calculations are included in Table 3.

According to Table 3, the strain hardening exponent decreased with the addition of alumina particles to the composite. This could be due to the decrease in the precipitation rate, which is in agreement with the microstructural observations and microhardness measurements. Additionally, the strain hardening exponent increased with the rise in heat treatment temperature, indicating an acceleration of precipitation.

Hollomon equation:

$$\sigma = K\,\varepsilon^{n} \tag{1}$$

σ is the true stress at the point, K is the initial strength coefficient, ε is the plastic strain at the point, and n is the strain hardening exponent of the point.

$$R^2 = 1 - \frac{SSR}{SST} \tag{2}$$

In the equation above, SSR is the sum of squared errors, SST is the sum of squared dispersion of the data about the mean, and R^2 is the coefficient of determination.

$$\varepsilon_{plastic} = \varepsilon_{true} - \frac{\sigma_{true}}{E} \tag{3}$$

In the equation above, $\varepsilon_{plastic}$ is the true plastic strain, ε_{true} is the true strain, σis the true elastic strain for the point in question, and E is Young's modulus.

TABLE 3. Strain hardening exponent and other data obtained from the Hollomon equation

Sample	n	K (MPa)	R^2
AA1050-AA2024 composite (6 cycles ARBed)	0.482609	1367.491	0.984
AA1050-AA2024-Al_2O_3 composite (created by the 6 cycles ARB)	0.88913	268.8285	0.996
AA2024	0.223913	361.3438	0.942
AA1050	0.186957	231.8743	0.945
AA2024-Precipitated	0.26087	418.9318	0.933
AA1050-AA2024 composite (heat treated at 110°C for 1 h)	0.963043	311.6721	0.951
AA1050-AA2024 composite (heat treated at 110°C for 3 h)	0.334783	1017.371	0.987
AA1050-AA2024 composite (heat treated at 110°C for 5 h)	0.852174	2131.045	0.939
AA1050-AA2024 composite (heat treated at 110°C for 10 h)	0.704348	1585.431	0.948
AA1050-AA2024-Al_2O_3 composite (heat treated at 110°C for 3 h)	0.371739	756.8921	0.978
AA1050-AA2024-Al_2O_3 composite (heat treated at 110°C for 10 h)	0.815217	5175.217	0.969
AA1050-AA2024-Al_2O_3 composite (heat treated at 110°C for 1 h)	0.519565	2470/673	0.993
AA1050-AA2024-Al_2O_3 composite (heat treated at 110°C for 5 h)	0.408696	485.6976	0.972
AA1050-AA2024-Al_2O_3 composite (heat treated at 150°C for 30 min)	0.926087	2864.428	0.936
AA1050-AA2024-Al_2O_3 composite (heat treated at 150°C for 1 h)	0.445652	652.8468	0.963
AA1050-AA2024-Al_2O_3 composite (heat treated at 150°C for 3 h)	0.778261	4463.812	0.981
AA1050-AA2024-Al_2O_3 composite (heat treated at 150°C for 10 min)	0.630435	877.5192	0.966
AA1050-AA2024-Al_2O_3 composite (heat treated at 190°C for 10 min)	0.297826	563.104	0.975
AA1050-AA2024-Al_2O_3 composite (heat treated at 190°C for 30 min)	0.667391	3850.2	0.957
AA1050-AA2024-Al_2O_3 composite (heat treated at 110°C for 1 h)	0.741304	3320.937	0.96
AA1050-AA2024-Al_2O_3 composite (heat treated at 190°C for 3 h)	0.593478	1838.103	0.954

Figure 15 shows the fracture surface of AA1050\AA2024 (a to e) and AA1050\AA2024\Al_2O_3 (f to j) composites after heat treatment at 110 °C. These images were taken from the fracture surface after the tensile test. In images of the fracture surface, it can be seen that, before heat treatment, a significant gap formed between the aluminum layers. Separation of the connected layers during ARB reduces the tensile strength and elongation. However, with heat treatment, the layer separation was significantly reduced. That indicates an improvement in bonding by heat treatment.

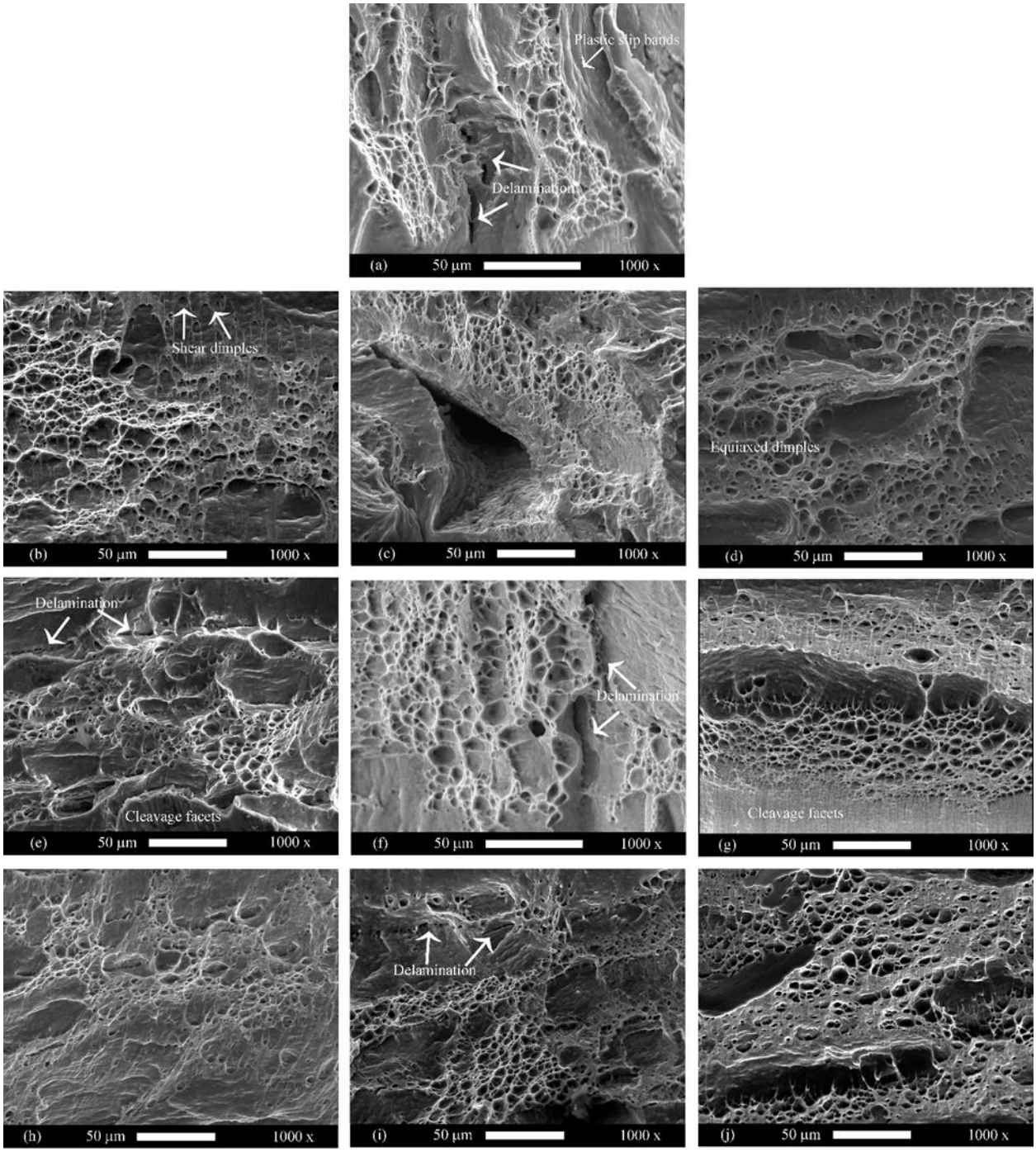

Figure 15. The image of the fracture surface of AA1050\AA2024 composites after heat treatment at 110 °C for a) 0, b) 60, c) 180, d) 300, and e) 600 min and the fracture surface image of composites AA1050\AA2024\Al_2O_3 after heat treatment at 110 °C for f) 0, g) 60, h) 180, i) 300 and j) 600 min

Holes, plastic strain bands, and cleavage surfaces were observed in all fracture surfaces. Cleavage surfaces indicate a brittle fracture, and holes and plastic strain bands indicate soft failure. Also, the reduction in hole size indicates a reduction in soft fracture. The change in the ratio of soft and brittle fracture surfaces in different samples occurred according to the elongation of Figure 14. In this way, comparing the heat-treated composites for 300 min that had the highest elongation, the AA1050\AA2024\$Al_2O_3$ composites' fracture surface had more holes and a larger volume than the AA1050\AA2024 composite. The difference in the fracture surface is proportional to the elongation of the two composites. Thus, the elongation of AA1050\AA2024\$Al_2O_3$ composite was more than AA1050\AA2024.

4. DISCUSSION

4. 1. Microstructure The AA2024 layers broke after the initial stages of ARB in the AA1050 field. This behavior can be explained by the hardness of AA2024 and AA1050, as different hardnesses result in different strain behavior (40). As a result, the AA2024 layers exhibited slower strain due to their higher hardness and broke at a rate equal to the strain applied by rolling (Figure 4). Consequently, the breaking caused the strain applied by rolling to pass around the AA2024 pieces with AA1050 flux. Therefore, the AA2024 thickness fragments were more than 10 times the theoretical amount.

According to Figure 4, some layers failed at 45°, a phenomenon associated with shear bands. Aluminum, with its FCC crystal system, has 12 slip systems. In the early stages of ARB, the strain of aluminum alloys occurred in a ductile form. However, the AA2024 layers suffered work hardening when subjected to further strain during successive rolling. They broke at an angle of 45°, at which the shear stress is highest. A more brittle fracture was observed in the AA1050\AA2024\Al_2O_3 nanocomposite. The presence of alumina nanoparticles between the AA1050 and the AA2024 layers increased work hardening. In the AA1050\AA2024 nanocomposite, ductile fractures, including the necking of the AA2024 layers, were observed due to the absence of alumina nanoparticles.

As shown in Figure 4, the AA2024 layers became thinner as strain was applied during several ARB stages. In this way, the 45° angle for the layers became smaller. However, the heads of AA2024 layers had a greater angle due to their high work hardening. Work hardening was applied during the breaking of the AA2024 and the flowing of the AA1050 layers. As a result, some heads of AA2024 pieces could withstand the force of rolling.

The AA2024 fragments' length in the AA1050\AA2024 composite was almost twice that of AA1050\AA2024\$Al_2O_3$. This event can be explained as alumina nanoparticles further work-hardening the AA1050\AA2024\$Al_2O_3$ nanocomposite in the AA2024 layers. Therefore, more brittle failures occurred in these layers.

By performing each rolling stage with a 50% reduction in thickness, the sheet's length doubles. Increasing the sheet length improves the distribution of reinforcing particles. A composite with uniform distribution is created by stacking composite layers in different stages of ARB. Reducing the thickness and increasing the sheet length during ARB decreases the concentration of reinforcing particles (41, 42). From Figure 5, it can be seen that the alumina particles penetrated deeper into the AA1050 matrix. Aluminum alloy 2024 is 4 times harder than aluminum alloy 1050. As a result, alumina nanoparticles penetrated AA1050 layers more than AA2024 layers during rolling.

In the microscopic images of Figures 4 and 5, alumina particles were not observed; however, their effect was evident as increased oxygen concentration in the SEM images. The primary alumina particles consist of agglomerated alumina nanoparticles (34). During successive rolling, applied pressure and strain separate and disperse these nanoparticles in the field (41, 42).

Rihanian et al. (22) proposed Equation 4 to determine the required thickness reduction in the ARB process to achieve a uniform distribution of reinforcing particles in the metal matrix. In Equation 4, f, d, and t_0 indicate the volume ratio, particle size, and initial thickness of metal sheets. In the present project, sheets with a thickness of 700 µm, reinforcing particles with a volume ratio of 0.00005, and particle size with a diameter or thickness of less than 100 nm were used. Based on Equation 4, a thickness reduction of 98% was necessary to achieve a proper distribution of reinforcing particles. This 98% thickness reduction was accomplished by performing six ARB steps, thereby ensuring a uniform distribution of reinforcing particles.

$$R = 1 - \left(\frac{\sqrt{3}\pi}{8f}\right)^{\frac{1}{3}} \left(\frac{d}{t_0}\right) \quad (4)$$

It is worth noting that, even with 0.5% by volume of copper oxide (CuO) nanoreinforcement particles in the aluminum matrix, we were unable to achieve proper distribution after 6 or 7 ARB stages (3, 9). Therefore, we tried using a much smaller amount of nanoreinforcement particles, this time alumina.

Various types of precipitates, such as T-phase, $Al_{77}Cu_{10}Fe_7Mn_5Si_2$, $Al_{79}Cu_{13}Fe_5Mn_2Mg_{0.7}Si_{0.2}$, and $Al_{65}Cu_{17}Mg_{18}$, exist intrinsically in AA2024. Most of these precipitates are larger than 100 nm, and their volume and number decreased after annealing. Heat

treatment for 30 minutes at 190 °C resulted in the formation of S' (Al_2CuMg) nanometer-sized precipitates. S' precipitates in the ARB process cause further structure modification due to nanometer precipitates having a higher surface-to-volume ratio (4, 9). These cases are shown in Figures 8 and 10, respectively.

Rolling causes an increase in work hardening, an increase in large angular boundaries, and UFG structure formation. These phenomena can be explained as follows:

In the ARB process, a potent strain is applied to the sheets. The strain applied during ARB increases the density of dislocations, and further, sub-grain structures are trimmed, and then large-angle grain boundaries are formed by the dislocations being ordered. Also, dislocations join the existing boundaries and increase the misorientation angle. Also, reducing layer thickness decreases grain width. As the length increases, the boundaries are stretched. Therefore, many dislocations must be created to increase the length of the boundaries (9, 43).

The processes mentioned in the previous paragraph always occur in ARB. However, three factors in this research caused the intensity of possible processes in ARB. These include:

- Carrying out the aging process
- Use of reinforcing particles
- Creation of a layered composite

The carried-out aging formed nanometer precipitates. Due to the semi-coherent nature of the precipitates generated during the aging, many dislocations are created at the boundary between the precipitates and the AA2024 fragments. These dislocations in the ARB process increase structural modification and further grain refinement (31).

Two metals with different strain behaviors are rolled together to create a layered composite. This process generates shear strain, a key factor in increasing work hardening and further modifying the structure (44, 45).

Many investigations have been done in creating metal composites with ceramic reinforcing particles using the ARB method (23, 46). The use of reinforcing particles increases work hardening, such as through aging and the formation of a layered composite. TEM images showed that using a minimal amount of nanometer-sized reinforcing particles significantly affects the microstructure. The effect of nanometer reinforcing particles is due to their high surface-to-volume ratio. In the composite of reinforcing particles and the metal matrix, the surface of the reinforcing particles has the main interaction with the metal matrix. Thus, dislocations are created by applying a strain. Of course, given the low percentage of reinforcing particles in the present project, the interaction between reinforcing particles and dislocations during stretching cannot be considered an important factor in increasing tensile strength. Therefore, the primary role of reinforcing particles in the current project is to help modify the composite structure.

Much research has used one or two of the mentioned factors, along with the ARB method. However, in creating the AA1050\AA2024\Al_2O_3 composite, all three factors were used along with the ARB method. In this way, contrary to the usual observations regarding the ARB aluminum grains (which were elongated), the uniaxial grains of aluminum were observed in Figures 9(a) and 9(b). However, elongated grains were created in the rolling orientation in the AA1050\AA2024 composite, which did not use reinforcing particles (Figures 9 (d) and 9(e)). Aluminum has a relatively high SFE (160-250 $mJ.m^{-2}$) (47). In this way, the dislocations created in the aluminum structure are recovered and removed more easily than in metals such as copper, which has an SFE of 70-78 ($mJ. m^{-2}$) (48). As a result, the copper grains will be uniaxial after ARB under the same conditions, whereas the rolled aluminum grains will be stretched in the rolling direction. However, in this project, further grain refinement was achieved by combining three factors with the ARB process: precipitation, reinforcing particles, and the formation of a layered composite, resulting in uniaxial aluminum grains.

After six cycles of ARB, all types of precipitates, including nanometer-sized precipitates, remained present in the AA2024 layers. Some studies have reported that precipitates, such as Al_3Sc, can be dissolved in the metal matrix during several ARB cycles (49). According to the observations and conclusions of these studies and the present research, precipitate dissolution in the field during ARB processing depends on precipitate characteristics and constituent elements. So, the two-component Al_3Sc precipitates dissolve in the aluminum field due to strong strain. However, the three-component S' or more complicated precipitates such as T-phase, do not dissolve. Because, in the dissolution of precipitates of AA2024, the bond between copper and magnesium (and other elements such as Mn and Fe) must be lost, in addition to the bond between copper and aluminum. Also, copper metal has larger atoms than scandium, which makes it more difficult for copper to penetrate the aluminum matrix.

SEM images showed that aging occurred faster in the AA1050\AA2024 composite than in the AA1050\AA2024\Al_2O_3 composite. Precipitation is highly dependent on vacancies. However, the reinforcing particles absorb the vacancies at heat treatment (32), reducing the vacancy density and delaying aging. Surprisingly, these changes were observed using 0.005 vol.% of alumina. Therefore, using only 0.005 vol.% alumina makes the structure more heat-stable.

4. 2. Mechanical Properties In the microstructure section, it was observed that the AA1050\AA2024\Al_2O_3 composite with a nanometer-scale microstructure was produced by performing 6 ARB stages. Also, it was observed that the use of 0.005 vol.% alumina in the raw materials significantly affects the final composite's microstructure. In addition, 30 minutes of aging at 190 °C resulted in the formation of nanometer-sized precipitates. In this section, the composites created by the ARB method were subjected to various heat treatments. Then, their mechanical properties were discussed and analyzed.

Heat treatments performed on AA1050\AA2024 composites caused a slight decrease in the microhardness of AA1050 (Figure 12). The temperatures chosen for the heat treatment were lower than those required to cause recrystallization in aluminum (greater than 230 °C) (7, 50). Therefore, it did not affect the composite microstructure produced by the ARB method. Because the AA1050 alloy is almost pure and cannot age harden (51), it can be concluded that the heat treatments did not cause significant recovery and only caused some softening. Therefore, it can be concluded that the heat treatment did not cause apparent recovery in AA1050.

Despite the discussions in the previous paragraph, the microhardness of the AA2024 layers varied after the composites were held at different temperatures and for different times. These changes occurred due to post-age hardening (post-aging) in the AA2024 layers. ARB caused the increase and decrease in microhardness compared to annealed alloys (28, 29, 52) to occur in less time (at least 6 hours earlier). Rolling causes many defects, such as dislocations, in the metal. Also, ARB reduced grain size and, as a result, increased grain boundary length. Dislocations and grain boundaries serve as penetration paths, thereby increasing the precipitation rate. For this reason, precipitation has reached its maximum impact on hardness at lower temperatures and shorter times.

With aging, at 190 °C and 150 °C, the hardness of AA2024 decreased slightly due to some recovery. However, with increasing aging time and increasing precipitation, the hardness of AA1050\AA2024\Al_2O_3 composites increased. At 110 °C, initial recovery did not occur due to the low temperature, and the maximum hardness from age hardening occurred later than at higher temperatures.

Using alumina at this temperature resulted in greater hardness stability with increasing aging time. The boundary between the reinforcing particles and the metal field is suitable for precipitation because there is no metallurgical connection. By carrying out precipitates in these areas, the linkage of reinforcing particles to the base metal was improved. Improvement in linkage can be demonstrated by increased tensile strength (Figure 14). As a result, the effect of reinforcing particles (despite their small amount) on hardness was demonstrated.

It can also be said that reinforcing particles increase grain refinement (Figure 9). The increase in grain refinement causes an increase in precipitation sites. Therefore, precipitation in the composite with alumina occurred more homogeneously. As a result, the hardness of the AA1050\AA2024\Al_2O_3 composite was more stable than that of AA1050\AA2024 with increasing heat treatment time. At 110 °C, with further aging, age hardening exceeded its optimal level, and the samples became over-aged. In this case, the hardness decreased due to increased brittle precipitates in the base metal and decreased toughness.

In the research by Zheng et al. (28), aluminum alloy 2024 was subjected to three ARB stages and a rolling stage with a 50% thickness reduction. The equivalent strain introduced during the process was 3.2. By aging for about 50 hours at 100 °C, they achieved the same hardness as the maximum hardness of AA2024 in our project. As shown in Figure 12, aging for 60 min (1 hour) at 110°C on the AA1050\AA2024 composite and 300 min (5 hours) at 110°C on the AA1050\AA2024\Al_2O_3 composite resulted in a hardness of 200 HV. However, in Zheng et al.'s(28), 50 hours of aging at 100 °C were used to achieve a similar hardness. The aging temperature in our project was 10 °C higher. However, this amount is not enough to account for this large difference.

Two main factors caused the significant difference in microhardness between the two projects.

• Apply strain 4.8 in our project

• Creating a composite between two alloys AA1050 and AA2024 in our project

The higher strain applied in our project resulted in more dislocations in the AA1050/AA2024 composites. This, in turn, resulted in the formation of more sub-grain structures in the AA1050\AA2024 composites, created with a strain of 4.8, which have more paths for atoms to penetrate, leading to a higher maximum hardness due to age hardening compared to AA2024 subjected to the strain of 3.2.

The strain behavior of two aluminum alloys, 2024 and 1050, differs. The difference in strain between these two alloys is evidenced by the fragmentation of AA2024 layers after several rolling steps (Figure 4). Creating AA1050\AA2024 composites causes friction between AA2024 and AA1050 layers. Consequently, more dislocations and sub-grain structures have been created in alloys, facilitating the penetration of copper and magnesium atoms and accelerating the age-hardening process.

As shown in Figure 12, despite the creation of a finer grain structure in the AA1050\AA2024\Al_2O_3 composite than in the AA1050\AA2024 composite (Figure 9), and despite the fact that the alumina particles are much harder

than aluminum, the AA1050\AA2024 composite reaches maximum hardness earlier than the AA1050\AA2024\$Al_2O_3$ composite. This can be explained by the fact that reinforcing particles promote the absorption and elimination of dislocations and vacancies during heat treatment (32). Vacancies and dislocations, which are mainly generated during rolling, serve as sites for precipitate nucleation during aging. By using ceramic particles and removing nucleation sites, precipitation proceeds at a lower rate. Thus, the AA1050\AA2024 composite reached its maximum hardness after 60 min, and the AA1050\AA2024\$Al_2O_3$ composite after 300 min of aging at 110 °C.

We intended to model and analyze the age hardening with models such as Avrami (Equation 5 (53)). However, due to the close hardness of the AA1050-AA2024/Al_2O_3 composites, we were unable to analyze the hardness based on these models. Because the hardness difference in the denominator becomes an odd number. This could indicate that alumina particles prevent age hardening. Thus, alumina slowed down the precipitation and reduced the changes in hardness. However, for the AA1050-AA2024 composite, modeling was performed. The numbers calculated based on the Avrami equation for 1, 3, and 5 hours were 1.00, 0.524, and 0.238, respectively. These numbers indicate the peak age hardening at 1 hour of heat treatment and the entry into the hyper-age hardening range at subsequent times.

$$X(t) = \frac{H(t)-H_o}{H_{max}-H_o}, 0 \le X \le 1 \quad (5)$$

Microhardness results of composites treated at different temperatures and times, the strain hardening exponent calculated by the Hollomon method, and Avram fitting, all proved the effect of precipitation reduction using alumina powder. Of course, in other studies, Chen et al. (32) and Karakas (54) also demonstrated a reduction in the precipitation rate and density of precipitates by using alumina fibers and boron carbide particles in the aluminum matrix.

According to Figure 14, performing six ARB stages has caused significant changes in elongation and tensile strength in AA1050\AA2024 composites and AA1050\AA2024\Al2O3 compared to annealed aluminum alloys 1050 and 2024. To understand this, one should have paid attention to the following points. The AA2024 layers became fragmented in the AA1050 field by performing several ARB cycles. Consequently, most of the tension was applied to the AA1050 continuous matrix. Because of this, the tensile strength decreased compared to AA2024 (about 40% decrease). However, by performing several stages of ARB, a UFG microstructure was formed (Figure 9). Also, substantial work hardening was imparted to the composite during successive rolling (7). In this way, the strength of AA1050\AA2024 composites was more than two times that of the annealed aluminum alloy 1050.

By performing heat treatment, three things happened in the composites over time:

- Reduction of work hardening
- Reaching the optimal condition of age hardening
- Over aging

Decreasing work hardening first caused a decrease in tensile strength. Then, upon reaching the optimal age hardening point, the tensile strength increased due to optimal precipitation. In this case, the precipitates acted as a barrier against dislocations and the formation of cracks. The tensile strength decreased due to the formation and growth of a network of brittle precipitate phases with increased aging time (6, 55). The rate of change in composites aged at 190 and 150 °C was higher than at 110 °C due to the higher temperature. For this reason, the maximum strength and maximum elongation of AA1050\AA2024\Al_2O_3 composites occurred in less time.

The composites aged at 110 °C, which is lower than the typical age-hardening temperature (44). As a result, there is less possibility of long-range penetration, more uniform precipitates were created (Figure 11), and excessive growth of rough precipitates was prevented. For this reason, those composites' maximum elongation and tensile strength were more significant than those of the aged composites at temperatures of 150 and 190 °C.

Comparing the elongation and tensile strength of two composites of AA1050\AA2024 and AA1050\AA2024\Al_2O_3 aged at 110 °C, the tensile strength and total elongation of the composite containing alumina were higher. This finding contrasted the results obtained before the aging process (3, 9). The post-aging process improved the bonding of reinforcing particles to the base metal and led to the formation of precipitates. As a result, these particles acted as barriers to dislocation movement and crack propagation. Therefore, the elongation and tensile strength improved.

The maximum total elongation and tensile strength for some composites created in this study and similar studies are shown in Table 4. The most similar study in Table 4 was conducted by Daneshvar et al. (56). In that research, an Al/Ni/Fe_3O_4 composite was created with 8 stages of ARB. In Daneshvar et al.'s (56) study, the nickel layers were broken in the aluminum field due to the strain behavior differences between nickel and aluminum. For this reason, the tensile strength of this composite was determined based on that of aluminum. Work hardening did not decrease due to the lack of heat treatment after ARB. As a result, the total elongation of this composite was less than 10%. Of course, due to the lack of aging capability in the Al/Ni/Fe_3O_4 composite, the improvement in particle bonding to the metal matrix and the layers together was not achievable through low-temperature heat treatment.

In another study, Mo et al. (57) developed an AA1100/AA7075 composite with 4 ARB stages with 30

min heat treatment at 460 °C before each cycle. They then performed a rolling step with a reduced thickness, similar to ARB, at ambient temperature. The tensile strength of the AA1100/AA7075 composite was 35% higher than the composite created in our research (AA1050\AA2024\Al_2O_3 aged at 110 °C). However, the total elongation of the AA1100/AA7075 composite was 65% lower than that of the AA1050/AA2024/Al_2O_3 composite. In the research done by Mo et al. (57), heat treatment was performed before each rolling stage.

Therefore, necking and layer breaking were prevented. In this way, preheating disrupts the grain-refinement process, and the contribution of UFG structures to improving tensile strength is reduced (7). However, much work was put into the sample by performing a cold rolling step after ARB. Also, because the dislocations created during a rolling step (work hardening) do not participate in forming sub-grains or strengthening grain boundaries (7, 9), they cause a significant reduction in elongation.

Additionally, Table 4 presents the results obtained with varying amounts of alumina. Ahmadi et al. (58) achieved a significant tensile strength of 270 MPa using 1.6 vol% alumina and 0.5 vol% silicon carbide, and performing 8 ARB steps. However, the total elongation of the composite they created was only 7%. In another study, Rezayat et al. (59) created an aluminum composite containing 3 vol% alumina by performing 8 ARB steps. They also achieved a tensile strength of 260 MPa and a total elongation of 4.5%. Reihanian et al. (22) created a composite with a strength of 160 MPa and a total elongation of 1.5% by increasing the alumina content to 4 vol%. As a result of the studies conducted, it can be said that reinforcing particles can delay crack formation and increase tensile strength. However, on the other hand, they contribute to crack growth once they have occurred and reduce ductility. The reduction in ductility caused by the use of high-volume reinforcing particles is attributed to the incoherency of ceramic particles in a metal matrix and stress concentration at the particle-matrix boundary. Incoherency and stress concentration also lead to a decrease in tensile strength when excessive alumina is used.

In creating the AA1050\AA2024\Al_2O_3 composite using the ARB method, we allowed the generated dislocations to organize during continuous rolling at ambient temperature, forming sub-granular structures or joining boundaries (Figure 9) (3). As a result, the elongation and impact of the grain boundaries increased, improving the tensile strength. Also, by performing heat treatment after ARB, we reduced work hardening, increased elongation, and promoted the formation of precipitates in the metal matrix (Figure 11), thereby improving the bonding of the composite components and increasing microhardness and tensile strength. As a result, we achieved higher elongation and appropriate tensile strength using a much smaller amount (approximately 200 times less) of alumina than in similar studies.

TABLE 4. Maximum tensile strength and total elongation for some composites created in our research and in other similar researches

Composite	Number of ARB cycles	UTS (MPa)	Total elongation (%)	Treatment after the ARB process	Description	Reference
Al/Ni/Fe_3O_4	8	150	8	-	ARB at ambient temperature	(56)
AA1050\AA2024\Al_2O_3	6	198	14	Aging at 110 °C	ARB at ambient temperature	This work
AA1050\AA2024	6	190	12	Aging at 110 °C	ARB at ambient temperature	This work
Al/Cu/Sn	7	140	11	-	ARB at ambient temperature	(44)
AA1100/AA7075	4	270	5	Rolling with 50% thickness reduction at ambient temperature	ARB with 30 min preheating at 460 °C	(57)
Al/Al_2O_3/SiC	8	270	7	-	1.6 vol.% alumina and 0.5 vol.% SiC	(58)
Al/Al_2O_3	8	260	4.5	-	3 vol.% Al_2O_3	(59)
Al/Al_2O_3	6	160	1.5	-	4 vol.% Al_2O_3	(22)

5. CONCLUSION

In this investigation, we created AA1050 (66 vol.%) \ AA2024 (34 vol.%) nanocomposites with aged AA2024 and through six ARB stages, with and without adding 0.005 vol.% of Al_2O_3 nanoparticles. It is noteworthy that the use of this negligible amount of reinforcing particles was studied for the first time. Then, for the first time, the hybrid-created composites were post-aged at 110, 150, and 190 °C. The following results can be obtained from the research:

- By performing some ARB stages, the layers of aluminum alloy 2024 were fragmented in the aluminum alloy 1050 field.

- The use of 0.005% vol.% of alumina caused the creation of a uniaxial microstructure in AA1050\AA2024 nanocomposites.
- The microhardness test results showed that the microhardness of AA1050 and AA2024 increased by about 60% and 45%, respectively, by performing six ARB stages.
- Examining the microhardness results showed that performing six stages of ARB increased the age-hardening rate by 10 times.
- Microhardness results showed that lowering the aging temperature and using reinforcing particles reduced the age-hardening rate.
- Microhardness test results showed that the AA1050\AA2024\Al_2O_3 composite was more heat-stable at 110 °C than the AA1050\AA2024 composite.
- Age hardening of AA1050\AA2024 composites resulted in significant improvements in elongation and tensile strength.
- The use of Al_2O_3 nanoparticles in the AA1050\AA2024 nanocomposite produced by the ARB method and aged at 110 °C resulted in improved elongation and tensile strength compared to the composite without reinforcing particles.

Acknowledgements

We also appreciate the financial support of the Iran National Science Foundation and the Research Deputy of the Sharif University of Technology under Grant No. QA030816

Ethics Approval and Consent to Participate

This article does not involve any studies with human participants or animals performed by any of the authors. Therefore, ethics approval and consent to participate are not applicable.

Competing Interests

The author declares no financial or organizational conflicts of interest.

Data Availability

The data that support the findings of this study are available upon reasonable request.

Declaration of Generative AI and AI-assisted Technologies in the Writing Process

During the preparation of this manuscript, the author used Grammarly exclusively for minor language editing to improve readability. After using this tool, the author carefully reviewed and edited the content as needed and takes full responsibility for the content of the published article.

Authors Biosketches

Dr. Hamed Roghani holds a Ph.D. in Materials Engineering with a specialization in nanomaterials and is currently a postdoctoral researcher in materials science. His research interests include the synthesis and characterization of carbide nanoparticles, self-propagating high-temperature synthesis (SHS), accumulative roll bonding, and metal forming processes. He has published several scientific papers in these areas.
Hamid Partoviar is a Ph.D. candidate in Materials Engineering at Iran University of Science and Technology and has successfully defended his research proposal. His research focuses primarily on metal forming and plastic deformation processes.
Dr. Hamidreza Jafarian is a faculty member in the Department of Materials Engineering at Iran University of Science and Technology. His research interests include metal forming, corrosion, and surface engineering, and he has published numerous papers in international scientific journals.
Prof. Seyed Khatiboleslam Sadrnezhaad is a professor of materials science and engineering at Sharif University of Technology and a prominent researcher in the field of materials science in Iran. He has an extensive record of research in metallurgy and materials science, particularly in nanomaterials and advanced materials, and has supervised many graduate students and published widely in international journals.
Dr. Ehsan Borhani is a faculty member at the University of Semnan in the field of Materials Engineering. His research interests include metal forming, nanomaterials, and related processing methods in materials science.

REFERENCES

1. Kumar K, Ingole SB, Saeedjassim A, Yatika Gori, Kaushik A, Kumar D, Jain A. Aluminum-foam by powder metallurgy: a review. Materials Today: Proceedings. 2023. https://doi.org/10.1016/j.matpr.2023.03.344
2. Li S, Yue X, Li Q, Peng H, Dong B, Liu T, Yang H, Fan J, Shu S, Qiu F, et al. Development and applications of aluminum alloys for aerospace industry. Journal of Materials Research and Technology. 2023;27:944-83. https://doi.org/10.1016/j.jmrt.2023.09.274
3. Roghani H, Borhani E, Shams SAA, Lee CS, Jafarian HR. On the microstructure, texture and mechanical properties through heat treatment in Al-CuO nanocomposite fabricated by accumulative roll bonding (ARB). Materials Science and Engineering: A. 2021;828:142080. https://doi.org/10.1016/j.msea.2021.142080
4. Chen X, Marioara CD, Andersen SJ, Friis J, Lervik A, Holmestad R, Kobayashi E. Precipitation processes and structural evolutions of various GPB zones and two types of S phases in a cold-rolled

Al-Mg-Cu alloy. Materials and Design. 2021;199:109425. https://doi.org/10.1016/j.matdes.2020.109425

5. Gholami MD, Hashemi R, Sedighi M. The effect of temperature on the mechanical properties and forming limit diagram of aluminum strips fabricated by accumulative roll bonding process. Journal of Materials Research and Technology. 2020;9:1831-46. https://doi.org/10.1016/j.jmrt.2019.12.016
6. Ghosh KS. Calorimetric studies of 2024 Al-Cu-Mg and 2014 Al-Cu-Mg-Si alloys of various tempers. Journal of Thermal Analysis and Calorimetry. 2019;136:447-59. https://doi.org/10.1007/s10973-018-7702-0
7. Roghani H, Borhani E, Shams SAA, Lee CS, Jafarian HR. Effect of concurrent accumulative roll bonding process and various heat treatment on the microstructure, texture and mechanical properties of AA1050 sheets. Journal of Materials Research and Technology. 2022;18:1295-306. https://doi.org/10.1016/j.jmrt.2022.03.001
8. Partoyar H, Jafarian HR, Roghani H, Mohammadzadeh A, Heidarzadeh A. Friction stir processing of AA1050/AA5052 composite produced by accumulative roll bonding process: microstructure and mechanical properties. Journal of Advanced Joining Processes. 2025;11:100306. https://doi.org/10.1016/j.jajp.2025.100306
9. Roghani H, Borhani E, Jafarian HR. Effect of a trace amount addition of CuO on aluminum sheet processed by accumulative roll bonding with the common roots and rapid annealing. Journal of Materials Research and Technology. 2021;15:4257-71. https://doi.org/10.1016/j.jmrt.2021.10.055
10. Sajjadi Nikoo S, Qods F, Yousefieh M. Microstructure evolution and mechanical properties of the AA2024/AA5083 ultra-fine grained composite fabricated via accumulative roll bonding (ARB) method. Journal of Materials Research. 2023. https://doi.org/10.1557/s43578-023-00985-z
11. Ebrahimi M, Wang Q. Accumulative roll-bonding of aluminum alloys and composites: an overview of properties and performance. Journal of Materials Research and Technology. 2022;19:4381-403. https://doi.org/10.1016/j.jmrt.2022.06.175
12. Farid W, Yu H. Developing aluminum matrix composites through microstructure optimization and particle reinforcement via ARB and cryorolling. Progress in Natural Science: Materials International. 2025. https://doi.org/10.1016/j.pnsc.2025.04.004
13. Jafarian HR, Mahdavian MM, Shams SAA, Eivani AR. Microstructure analysis and observation of peculiar mechanical properties of Al/Cu/Zn/Ni multi-layered composite produced by accumulative roll bonding (ARB). Materials Science and Engineering: A. 2021;805:140556. https://doi.org/10.1016/j.msea.2020.140556
14. Barakat WS, Younis MK, Sadoun AM, Fathy A, Habba MIA. Optimization of the accumulative roll bonding process parameters and SiC content for optimum enhancement in mechanical properties of Al-Ni-SiC composites. Alexandria Engineering Journal. 2023;76:131-51. https://doi.org/10.1016/j.aej.2023.06.027
15. Sadhu KK, Mandal N, Sahoo RR. SiC/graphene reinforced aluminum metal matrix composites prepared by powder metallurgy: a review. Journal of Manufacturing Processes. 2023;91:10-43. https://doi.org/10.1016/j.jmapro.2023.02.026
16. Moradi Faradonbeh A, Shamanian M, Edris H, Paidar M, Bozkurt Y. Friction stir welding of Al-B4C composite fabricated by accumulative roll bonding: evaluation of microstructure and mechanical behavior. Journal of Materials Engineering and Performance. 2018;27:835-46. https://doi.org/10.1007/s11665-018-3131-2
17. Pallathadka H, Ghazaly NM, Alhadrawi M, Atif M, Castagne XP. Electromagnetic and fracture properties of AA1100/Fe2O3 composite strips fabricated via ARB process. Powder Metallurgy and Metal Ceramics. 2024;63:280-91. https://doi.org/10.1007/s11106-025-00461-9
18. Motevali Emami S, Karbasi M, Amirkhani Dehkordi E. Enhancing electrochemical properties of Pb composite anode by the addition of W-Co3O4 ceramic particles fabricated by accumulative roll bonding. Ceramics International. 2025. https://doi.org/10.1016/j.ceramint.2025.04.311
19. Singh VP, Gupta GK, Mishra S. Evaluation of microstructure and mechanical properties of GO-reinforced multilayer Al5052 composite fabricated by accumulative roll bonding. JOM. 2025. https://doi.org/10.1007/s11837-025-07332-z
20. Golmohammadi M, Salehi M, Koohdar HR. Enhanced corrosion and tribological properties of GO-reinforced Cu matrix nanocomposites fabricated by ARB process. Metallurgical and Materials Transactions A. 2025;56:2074-89. https://doi.org/10.1007/s11661-025-07760-1
21. Nasresfahani MR, Shamanian M. Development and characterization of Al/MWCNT-Al2O3 hybrid composite by accumulative roll bonding. Journal of Materials Science. 2018;53:10812-21. https://doi.org/10.1007/s10853-018-2372-7
22. Reihanian M, Naseri M, Jalili Shahmansouri M. Effect of the particle size on the deformation and fracture behavior of Al/4vol.%Al2O3 composite produced by accumulative roll bonding (ARB). Iranian Journal of Materials Forming. 2015;2:14-26. https://doi.org/10.22099/ijmf.2015.3237
23. Bembalge OB, Panigrahi SK. Exploring a hybrid manufacturing process to develop high performance age hardenable ultrafine grained AA6063/SiC nano-composite sheets. Journal of Manufacturing Processes. 2021;70:508-17. https://doi.org/10.1016/j.jmapro.2021.09.003
24. Alphonse M, Bupesh Raja VK, Vivek MS, Sai Deepak Raj NV, Satya Sai Darshan M, Bharmal P. Effect of heat treatment on mechanical properties of forged aluminium alloy AA2219. Materials Today: Proceedings. 2021. https://doi.org/10.1016/j.matpr.2020.12.334
25. Wang SB, Liu ZR, Xia SL, Key J, Chen JH. Tetragonal-prism-like Guinier-Preston-Bagaryatsky zones in an AlCuMg alloy. Materials Characterization. 2017;132:139-44. https://doi.org/10.1016/j.matchar.2017.08.014
26. Partoyar H, Roghani H, Jafarian HR, Roshani M. Effect of preheating before rolling on the microstructural and mechanical properties of lamellar Al/Ti/Al composite produced by roll bonding. Results in Materials. 2024;23:100594. https://doi.org/10.1016/j.rinma.2024.100594
27. Roghani H, Borhani E, Ahmadi E, Jafarian H. Study of changes in the aging process, microstructure, and mechanical properties of AA2024-AA1050 nanocomposites created by the accumulative roll bonding process, with the addition of 0.005 vol.% of alumina nanoparticles. Discover Nano. 2024;19:1-18. https://doi.org/10.1186/s11671-023-03917-2
28. Zheng R, Bhattacharjee T, Shibata A, Tsuji N, Ma C. Effect of accumulative roll bonding (ARB) and subsequent aging on microstructure and mechanical properties of 2024 Al alloy. Materials Transactions. 2016;57:1462-70. https://doi.org/10.2320/matertrans.MH201512
29. Tsuji N, Iwata T, Sato M, Fujimoto S, Minamino Y. Aging behavior of ultrafine grained Al-2wt%Cu alloy severely deformed by accumulative roll bonding. Science and Technology of Advanced Materials. 2004;5:173-80. https://doi.org/10.1016/j.stam.2003.10.019
30. Rezaei MR, Toroghinejad MR, Ashrafizadeh F. Effects of ARB and ageing processes on mechanical properties and microstructure of 6061 aluminum alloy. Journal of Materials Processing Technology. 2011;211:1184-90. https://doi.org/10.1016/j.jmatprotec.2011.01.023

31. Azad B, Borhani E. The effect of Al2Cu precipitate size on microstructure and mechanical properties of Al-2wt.%Cu alloys fabricated by ARB. Journal of Materials Engineering and Performance. 2015;24:4789-96. https://doi.org/10.1007/s11665-015-1800-y
32. Chen KC, Chao CG. Effect of delta alumina fibers on the aging characteristics of 2024-based metal-matrix composites. Metallurgical and Materials Transactions A. 1995;26:1035-43. https://doi.org/10.1007/bf02670599
33. Cheng S, Zhao YH, Zhu YT, Ma E. Optimizing the strength and ductility of fine structured 2024 Al alloy by nano-precipitation. Acta Materialia. 2007;55:5822-32. https://doi.org/10.1016/j.actamat.2007.06.043
34. Roghani H, Borhani E, Jafarian HR, Yousefieh M, Naseri M, Ostovari Moghadam A. On the impact of using alumina nanoparticles and initial aging on the microstructure and mechanical properties of the AA1050/AA2024 nanostructure composite created by accumulative roll bonding (ARB) method. Wear. 2023;526-527:204895. https://doi.org/10.1016/j.wear.2023.204895
35. Zhou T, Babu RP, Hou Z, Hedstrom P. On the role of transmission electron microscopy for precipitation analysis in metallic materials. Critical Reviews in Solid State and Materials Sciences. 2022;47:388-414. https://doi.org/10.1080/10408436.2021.1941751
36. Klein ND, Hurley KR, Feng ZV, Haynes CL. Dark field transmission electron microscopy as a tool for identifying inorganic nanoparticles in biological matrices. Analytical Chemistry. 2015;87:4356-62. https://doi.org/10.1021/acs.analchem.5b00124
37. Dehghan M, Qods F, Gerdooei M, Mohammadian-Semnani H. Effect of inter-cycle heat treatment in accumulative roll-bonding (ARB) process on planar isotropy of mechanical properties of AA1050 sheets. Transactions of Nonferrous Metals Society of China. 2020;30:2381-93. https://doi.org/10.1016/S1003-6326(20)65386-9
38. Kang SK, Kim YC, Kim KH, Kwon D, Kim JY. Constitutive equations optimized for determining strengths of metallic alloys. Mechanics of Materials. 2014;73:51-57. https://doi.org/10.1016/j.mechmat.2014.01.010
39. Bowen AW, Partridge PG. Limitations of the Hollomon strain-hardening equation. Journal of Physics D: Applied Physics. 1974;7:969. https://doi.org/10.1088/0022-3727/7/7/305
40. Yousefi Mehr V, Rezaeian A, Toroghinejad MR. Application of accumulative roll bonding and anodizing process to produce Al-Cu-Al2O3 composite. Materials and Design. 2015;70:53-59. https://doi.org/10.1016/j.matdes.2014.12.042
41. Ramkumar KR, Dinaharan I, Murugan N, Kim HS. Development of aluminum matrix composites through accumulative roll bonding: a review. Journal of Materials Science. 2024;59:8606-49. https://doi.org/10.1007/s10853-024-09682-6
42. Yang Z, Ni Z, Yan J, Fan L, Zhang J, Chen X, Guan R. Towards high performance nano multilayered graphene/5052 Al composite: in situ interfacial tailoring via accumulative roll bonding. Carbon. 2025;238:120213. https://doi.org/10.1016/j.carbon.2025.120213
43. Gashti SO, Fattah-alhosseini A, Mazaheri Y, Keshavarz MK. Effects of grain size and dislocation density on strain hardening behavior of ultrafine grained AA1050 processed by accumulative roll bonding. Journal of Alloys and Compounds. 2016;658:854-61. https://doi.org/10.1016/j.jallcom.2015.11.032
44. Mahdavian MM, Khatami-Hamedani H, Abedi HR. Macrostructure evolution and mechanical properties of accumulative roll bonded Al/Cu/Sn multilayer composite. Journal of Alloys and Compounds. 2017;703:605-13. https://doi.org/10.1016/j.jallcom.2017.01.300
45. Sun HY, Du P, Wang ZJ, Ma M, Liu WC, Sasaki G, Zhang JX. Study on the microstructure, texture and mechanical properties of hot-rolled and T6-treated Al1060/Al6061-TiCp/Al1060 laminated composites. Journal of Materials Research and Technology. 2022;18:2808-21. https://doi.org/10.1016/j.jmrt.2022.03.180
46. Jamaati R, Toroghinejad MR, Hoseini M, Szpunar JA. Texture development in Al/Al2O3 MMCs produced by anodizing and ARB processes. Materials Science and Engineering: A. 2011;528:3573-80. https://doi.org/10.1016/j.msea.2011.01.056
47. Li Y, Yu L, Pang X, Qin G. Tuning stacking fault energy and enhancing mechanical properties of Al through Mg and Sc doping: insights from density functional theory. Materials Today Communications. 2025;43:111639. https://doi.org/10.1016/j.mtcomm.2025.111639
48. Devi Janani R, Salman SA, Pavithra Priyadharshini K, Karthik V. Effect of composition on the stacking fault energy of copper-nickel alloys using molecular dynamics simulations. Materials Today: Proceedings. 2021;39:1796-800. https://doi.org/10.1016/j.matpr.2020.07.737
49. Borhani E, Jafarian H, Terada D, Adachi H, Tsuji N. Microstructural evolution during ARB process of Al-0.2 mass% Sc alloy containing Al3Sc precipitates in starting structures. Materials Transactions. 2012;53:72-80. https://doi.org/10.2320/matertrans.MD201125
50. Reed-Hill RE, Abbaschian R. Physical metallurgy principles. PWS-Kent Publishing; 2008.
51. Kaufman JG, Rooy EL. Aluminum alloy castings: properties, processes, and applications. ASM International; 2004.
52. Afzal N, Shah T, Ahmad R. Microstructural features and mechanical properties of artificially aged AA2024. Strength of Materials. 2013;45:684-92. https://doi.org/10.1007/s11223-013-9504-8
53. Jonas JJ, Quelennec X, Jiang L, Martin E. The Avrami kinetics of dynamic recrystallization. Acta Materialia. 2009;57:2748-56. https://doi.org/10.1016/j.actamat.2009.02.033
54. Karakas MS. Effect of aging on the mechanical properties of boron carbide particle reinforced aluminum metal matrix composites. Middle East Technical University; 2007.
55. Shih HC, Ho NJ, Huang JC. Precipitation behaviors in Al-Cu-Mg and 2024 aluminum alloys. Metallurgical and Materials Transactions A. 1996;27:2479-94. https://doi.org/10.1007/bf02652342
56. Daneshvar F, Reihanian M, Gheisari K. Al-based magnetic composites produced by accumulative roll bonding (ARB). Materials Science and Engineering: B. 2016;206:45-54. https://doi.org/10.1016/j.mseb.2016.01.003
57. Mo TQ, Chen ZJ, Li BX, Wang PJ, Liu Q. Tailoring of interface structure and mechanical properties in ARBed 1100/7075 laminated composites by cold rolling. Materials Science and Engineering: A. 2019;755:97-105. https://doi.org/10.1016/j.msea.2019.03.075
58. Ahmadi A, Toroghinejad MR, Najafizadeh A. Evaluation of microstructure and mechanical properties of Al/Al2O3/SiC hybrid composite fabricated by accumulative roll bonding process. Materials and Design. 2014;53:13-19. https://doi.org/10.1016/j.matdes.2013.06.064
59. Rezayat M, Akbarzadeh A, Owhadi A. Production of high strength Al-Al2O3 composite by accumulative roll bonding. Composites Part A: Applied Science and Manufacturing. 2012;43:261-67. https://doi.org/10.1016/j.compositesa.2011.10.015

Persian Abstract

چکیده

در این پژوهش، کامپوزیت‌های چندلایه‌ی پایه آلومینیومی شامل آلیاژ AA1050 (به میزان ٦٦.٦ درصد حجمی) و آلیاژ AA2024 پیش‌پیرسخت‌شده (٣٣.٤ درصد حجمی) با افزودن مقدار ناچیزی از نانوذرات Al_2O_3 (به میزان ۰.۰۰۵ درصد حجمی) با استفاده از شش سیکل نورد تجمعی (ARB) با موفقیت ساخته شدند. سپس کامپوزیت‌ها برای بهینه‌سازی ریزساختار و خواص مکانیکی، تحت عملیات پیرسازی در دماهای ۱۱۰، ۱۵۰ و ۱۹۰ درجه سانتی‌گراد و برای زمان‌های مختلف (۰ تا ۱۰ ساعت) قرار گرفتند. برای ارزیابی مواد از میکروسکوپ نوری، میکروسکوپ الکترونی روبشی (SEM)، میکروسکوپ الکترونی عبوری (TEM)، آزمون ریزسختی و آزمون کشش استفاده شد. نتایج نشان داد که فرایند ARB در ترکیب با تقویت حداقلی توسط نانوذرات، به ریزدانه‌شدن قابل‌توجه منجر شد. افزایش چشمگیری در استحکام کششی (تا ۲۲۰ مگاپاسکال، معادل ۲۱۵ درصد افزایش نسبت به AA1050 آنیل‌شده) و شکل‌پذیری (١٤ درصد ازدیاد طول کل) از طریق ARB و پیرسازی پس از فرایند ARB حاصل شد. همچنین حضور نانوذرات آلومینا نه‌تنها فراپیرسازی را به تأخیر انداخت، بلکه موجب بهبود پیوند ذره–زمینه و پایداری ساختاری شد. این پژوهش رویکردی عملی برای طراحی و تنظیم کامپوزیت‌های آلومینیومی با کارایی بالا از طریق راهبردهای ترکیبی برای اصلاح ریزساختار، شامل ARB، پیرسختی و نیز به کمک نانوذرات ارائه می‌دهد.